Biomaterials 276 (2021) 121053

Contents lists available at ScienceDirect

Biomaterials

journal homepage: www.elsevier.com/locate/biomaterials

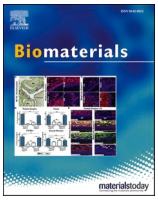

Construction and evaluation of novel αvβ3 integrin ligand-conjugated ultrasmall star polymer micelles targeted glomerular podocytes through GFB permeation

Chengyuan Huang, Xuan Zhao, Meiling Su, Zongning Yin *

Key Laboratory of Drug-Targeting and Drug Delivery System of the Education Ministry and Sichuan Province, Sichuan Engineering Laboratory for Plant-Sourced Drug and Sichuan Research Center for Drug Precision Industrial Technology, West China School of Pharmacy, Sichuan University, Chengdu, 610041, China

ARTICLE INFO

Keywords:
αvβ3 integrin
Star polymers
SET LRP polymerization
Glomerular podocytes
Dexamethasone acetate
Glomerular filtration barrier

ABSTRACT

As glomerular cells, podocytes are the last line of defense for glomerular filtration barriers (GFB) and play a critical role in chronic kidney disease (CKD). Podocyte-targeted drug delivery is a promising direction in the treatment of CKD. In this study, we constructed four-arm star polymers conjugated with a novel linear RWrNM peptide. And poly ε-caprolactone (PCL) hydrophobic core and brush poly (2-hydroxyethyl methacrylate) (PHEMA) hydrophilic shell were synthesized by ROP and SET LRP polymerization. The PHEMA modified by succinic anhydride was coupled with the novel linear RWrNM peptide, and then the PCL hydrophobic core was loaded with dexamethasone acetate (Dexac) to form micelles with stable dimensions. Our findings showed that the novel micelles had an ultrasmall particle size of 16–30 nm. We, for the first time, showed that the specific affinity of the novel linear RWrNM peptide to primary podocytes (24.9 ± 1.7 times of the free RhB uptake) through the αvβ3 integrin receptor mediation was comparable to that of B16F10 cells (24.4 ± 1.2 times of the free RhB uptake). In vivo studies showed that the novel ultrasmall micelles possessed a significant kidney-targeted effect, excellent podocyte colocalization effect, and GFB permeability at 49%–60 % in normal SD rats. Besides, the novel ultrasmall micelles decreased the plasma elimination half-life of Dexac to 1.62–2.09 h and showed good safety in vitro and in vivo. Both in vitro and in vivo results demonstrated the novel ultrasmall micelles could be used as a promising drug delivery strategy for actively targeted therapy of CKD.

1. Introduction

Kidney disease has been an urgent public health threat in the world [1,2]. It has been predicted that by 2040, chronic kidney disease (CKD) will lead to 3.09 million deaths. Under positive health conditions, this number will be controlled to 2.23 million, while it will rise to 4.05 million under the worst health conditions [3]. The current supportive therapy of CKD includes blood pressure/protein intake control, angiotensin-converting enzyme inhibitor (ACEI), ANG II receptor blockers (ARBs), immunosuppressants, and steroids [4–6]. Furthermore, synthetic glucocorticoids are still the standard treatment for proteinuria caused by CKD and nephrotic syndrome (NS), including micro-change disease (MCD), focal segmental glomerulosclerosis (FSGS), membranous nephropathy (MN), and immunoglobulin A nephropathy (IgAN) or subsequent complications due to diabetes or human immunodeficiency virus (HIV) infection [7–10]. However, long-term intake of high-dose systemic glucocorticoids may induce serious side effects, such as osteoporosis, cardiovascular disease, psychosis, immune response, reproductive damage, and growth retardation in children [11–17]. Therefore, it is necessary to further understand the structure and function of the kidney, clarify the pathogenesis of CKD, and develop safe and effective drug treatments to prevent the progression of CKD.

Drug delivery using nanotechnology is a novel and promising strategy in therapeutic medicine. Nanocarriers have been designed for the delivery of drugs and imaging substances to enhance pharmacokinetics and pharmacodynamics, and nanocarriers can be targeted to specific tissue cells in the disease site [18]. Recent research progress has proved that CKD is characterized by damage to podocytes in the glomerular filtration barrier (GFB) [19]. Podocytes are terminally differentiated cells derived from glomerular mesenchymal cells, and they cover the exterior of the glomerular capillaries and play a vital role in maintaining the integrity and function of GFB [20]. Targeted drug delivery to

* Corresponding author.
E-mail address: zongningyin@163.com (Z. Yin).

https://doi.org/10.1016/j.biomaterials.2021.121053
Received 3 December 2020; Received in revised form 25 July 2021; Accepted 26 July 2021
Available online 29 July 2021

podocytes may be an effective approach to treat kidney disease caused by podocyte damage [21,22]. Studies have shown that dexamethasone (Dex) can also directly act on glomerular podocytes, thereby exerting a protective effect [23–28]. However, GFB presents an obstacle to the therapeutic agent based on the charge and molecular size, leading to major difficulties in drug delivery to the kidney. Therefore, recent studies have been focused on different strategies to enhance the delivery of therapeutic agents across the GFB [29–31], while there is still a lack of more meaningful research progress in vivo, such as in vivo evaluation of GFB permeability, cell colocalization of nanocarriers in the kidney, pharmacokinetic parameters, pharmacodynamic evaluation, and so on.

The biggest difficulty in podocyte-targeted therapy is to design nanocarriers with suitable particle sizes to promote the permeation of drugs through GFB. GFB has a three-layer structure consisting of porous glomerular endothelial cells (pore size of 70–100 nm), glomerular basement membrane(GBM), and podocytes (with staggered foot processes forming 40-nm filtration slits) [32]. The latest studies on rat podocyte ultrastructure have shown that there are elliptical and circular pores in the filtration slits of normal podocytes, and the average size of these pores is about 24 nm [33–38], indicating that only ultrasmall nanocarriers can effectively pass through the GFB and eventually accumulate in podocytes. In glomerulonephritis, the integrity of the size and charge selection barrier is compromised, allowing larger nanocarriers (37.9 nm) and anionic polymers to cross the GBM or GFB [39,40].

Based on the special physiological structure of glomeruli and podocytes, we designed novel ultrasmall star polymer micelles that could permeate the GFB under normal physiological conditions and reach the podocytes. The rapid clearance of the kidney makes it difficult to achieve ideal targeted effects only through the passive accumulation of nanocarriers, while receptor-ligand-mediated actively targeted nanocarriers have great potential. αvβ3 integrin receptors positively expressed in podocytes are chosen as the targeted receptor [41–43]. In the integrin family, αvβ3 integrin is considered to be very effective for receptor-ligand-mediated nanocarriers delivery to cells [44]. We selected a novel linear RWrNM peptide with high affinity to αvβ3 integrin as the targeted ligand [45] and designed four-arm star polymers conjugated with the novel linear RWrNM peptide. And poly ε-caprolactone (PCL) core and brush-like poly (2-hydroxyethyl methacrylate) (PHEMA) hydrophilic shell were synthesized by ROP and SET LRP polymerization. After succinic anhydride modification, star polymer was coupled with linear RWrNM peptide to form dimensionally stable ultrasmall targeted micelles loaded with Dexac. We, for the first time, confirmed that the novel linear RWrNM peptide had a high affinity to primary podocytes at the cellular level, and it was comparable to B16F10 cells. In vivo studies using normal Sprague-Dawley (SD) rats indicated that the ultrasmall micelles had a significant kidney-targeted effect, excellent podocyte colocalization effect, and GFB permeability at 49%–60 %. Besides, the plasma elimination half-life of Dexac was decreased to 1.62–2.09 h, and the novel ultrasmall micelles showed good safety in vitro and in vivo.

2. Materials and methods

All solvents were of analytical grade. Pentaerythritol (98 %), ε-caprolactone (99 %), stannous octoate [$(Sn(Oct)_2$, 95 %], N,N,N′,N″,N‴-pentamethyldiethylenetriamine (PMDETA,99 %), 2-bromoisobutyryl bromide (2-BiBB,98 %), rhodamine B (RhB, 95 %), 1-(3-(dimethylamino)propyl)-3-ethylcarbodiimide hydrochloride (EDC-HCl, 98 %), N-hydroxysuccinimide (NHS, 98 %), dimethylaminopyridine (DMAP, 99 %), Dex (98 %) and Dexac (98 %) were purchased from Aladdin Corporation (Shanghai, China). Succinic anhydride (AR), hydrazine hydrate (80 %), and copper powder (AR) were provided by Kelon Chemical Industry (Chengdu, China). 2-Hydroxyethyl methacrylate (HEMA, 97 %) was supplied by Alfa Aesar Co. Ltd. (USA). To remove the stabilizer, HEMA was passed through the neutral alumina column. 6-Aminofluorescein (6-AF, 97 %) was obtained from McCarthy Reagent (Chengdu, China). Coumarin 6 (98 %) was purchased from J&K Scientific Ltd. RWrNM peptide (98 %) was custom synthesized by China Peptides Co. Ltd. (Shanghai, China). DMEM/F12 and RPMI-1640 medium were provided by Hyclone (Utah, USA). Trypsin-EDTA and Insulin-Transferrin-Selenium (ITS-G) were provided by Gibco (Grand Island, NY, USA). Penicillin-streptomycin solution, and 3-(4,5-Dimethylthiazol-2-yl)-2,5-diphenyltetrazolium bromide (MTT) were purchased from Biosharp (Hefei, China). β3 Integrin rabbit polyclonal antibody and Cy3-conjugated affinipure goat anti-rabbit IgG(H + L) were obtained from Proteintech (Wuhan, China). L02 cells were gifted by Professor Zhirong Zhang (West China School of Pharmacy, Sichuan University). DiD was provided by Keygenbiotech (Nanjing, China). SD rats were purchased from Chengdu Dashuo Animal Company (Chengdu, China). All animal-related experiments were approved by the Animal Care and Use Committee of Sichuan University.

2.1. Synthesis of 4sPCL-PHEMA-COOH-RWrNM

Detailed synthesis method for 4sPCL, 4sPCL-Br, 4sPCL-PHEMA, 4sPCL-PHEMA-COOH (4sPCHC), 4sPCL-PHEMA-COOH-RWrNM (4sPCHC/R), 6-aminofluorescein conjugated 4sPCHC/R, and RhB-RWrNM fluorescent probe was described in the supplementary materials.

2.2. Determination of critical micelle concentration

Pyrene acetone stock solution (30 μL, 60 μM) was added into a 4-mL centrifuge tube. After evaporation of the acetone, 3 mL micelles of different concentrations were added into the above-mentioned centrifuge tube and equilibrated at room temperature for 24 h in the dark. At an emission wavelength of 393 nm, a fluorescence spectrophotometer was used to scan the excitation wavelength at a speed of 200 nm/min from 300 to 400 nm with a slit width of 5 nm. A curve was drawn based on the ratio between the peak intensity after the redshift of the peak near 334 nm to the peak intensity before the redshift and the logarithm of the micelles concentration.

2.3. Preparation of Dexac-loaded micelles

DMF stock solution of Dexac (2 mL, 500 μg/mL) and star polymers (10 mg) were mixed thoroughly by ultrasonication for 5 min. The mixtures were added dropwise into 8 mL ultrapure water or PBS (pH 7.4), followed by stirring at 1200 rpm. Subsequently, micelles were dialyzed in a dialysis bag (MW cutoff 3500 Da) against ultrapure water or PBS (pH 7.4), and the dialysis medium was changed every 30 min. After 3 h, micelles were obtained, and the hydrodynamic diameters and zeta potential of micelles were measured by dynamic light scattering (DLS, Zetasizer Nano ZS90, England) and transmission electron microscope (TEM, JEM-2100Plus, Japan).

2.4. In vitro serum colloidal stability assay

The light transmittance analysis was used to evaluate the colloidal stability of nanocarriers [46]. The aggregation phenomenon of polymer micelles was evaluated in PBS (pH 7.4) containing 10 % FBS. A UV–Vis spectrophotometer (Varian Cary 100 Conc, Agilent, USA) was used to quickly scan 10 % FBS, Dexac-4s$PC_{21}H_{21}C$ micelles in PBS (pH 7.4) containing 10 % FBS, and Dexac-4s$PC_{21}H_{21}C/R_2$ micelles in PBS (pH 7.4) containing 10 % FBS within the wavelength range of 300–800 nm to determine the minimum light transmittance peak (λmin). Subsequently, the mixtures were incubated at 37 °C with shaking at 100 rpm. At predetermined time points (0, 0.25, 0.5, 1, 2, 3, 4, 5, and 6 h), 0.1 mL of the mixture was transferred to a 96-well plate. The light transmittance value was measured by a multifunctional microplate reader (Thermo Varioskan LUX, USA).

2.5. Leakage of Dexac from micelles in serum

Dexac-4sPC$_{21}$H$_{21}$C and Dexac-4sPC$_{21}$H$_{21}$C/R$_2$ were incubated with 50 % FBS at 37 °C with shaking at 100 rpm for 4 h. Then, the free Dexac solution was obtained from ultrafiltration devices. The concentration of free Dexac in the external tube was measured by HPLC analysis. The HPLC system was equipped with a Waters515 pump, Dikma C18 column, and Waters2487 ultraviolet detector. Detector wavelength was set at 240 nm, and the mobile phase was composed of methanol and water (70/30, v/v) at a flow rate of 1 mL/min at 30 °C.

2.6. In vitro drug release

DMF stock solution of Dexac (4 mL, 500 μg/mL) and star polymers (20 mg) were mixed thoroughly by ultrasonication for 5 min. The mixtures were added dropwise into 16 mL PBS (pH 7.4) and stirred at 1200 rpm. Subsequently, 2 mL drug-loaded micelles were transferred to a dialysis bag (MW cutoff 3500 Da) and dialyzed against 20 mL acetate buffer (pH 4.5). After reaching balance, the concentration of free Dexac in external dialysis fluid was measured by HPLC analysis. The drug loading content (DLC) and encapsulation efficiency (EE) were calculated by the following formula. Besides, 4 mL drug-loaded micelles was transferred into another dialysis bag (MW cutoff 3500 Da) and dialyzed against 40 mL PBS (pH 7.4), and the dialysis medium was changed every 30 min. After 3 h, the above-mentioned drug-loaded micelles were dialyzed against 40 mL acetate buffer (pH 4.5) at 37 °C with shaking at 100 rpm. At selected time points, 1 mL external dialysis fluid was withdrawn and replaced with an equal volume of acetate buffer (pH 4.5). The samples were analyzed by HPLC to measure the concentration of Dexac. There were three parallel samples in each group.

$$\text{EE}\ (\%) = \frac{\text{weight of drug added} - \text{weight of the drug in free}}{\text{weight of drug added}} \times 100\%$$

$$\text{DLC}\ (\%) = \frac{\text{weight of drug added} - \text{weight of the drug in free}}{\text{weight of (drug} - \text{loaded micelles)}} \times 100\%$$

2.7. Cell culture

2.7.1. Primary podocyte culture and identification

SD rats (age at 6–8 days) were selected. The kidney was aseptically dissected, the kidney capsule was peeled off, and the kidney was rinsed with PBS (pH 7.4) three times. The renal cortex was cut into small pieces of 1–2 mm^3 using ophthalmic forceps and then digested with 0.125 % trypsin at 37 °C for 10–15 min. Subsequently, DMEM/F12 complete medium supplemented with 10 % FBS, 0.5 % ITS-G, 100 U/mL streptomycin, and 100 U/mL penicillin were added to terminate the digestion. The digestion mixtures were passed through a 70-μm cell sieve with a 5-mL syringe plug. The 70-μm cell sieve was rinsed with DMEM/F12 complete medium, and then the digestion mixtures were passed through a 40-μm cell sieve. Finally, glomeruli on the 40-μm cell sieve were eluted with DMEM/F12 complete medium and cultured in a 100-mm petri dish (coated with 4 μg/cm^2 type I collagen) at 37 °C in a humidified atmosphere containing 5 % CO_2. When the cells were cultured to a confluence of 80–90 %, they were passaged by trypsin differential digestion, and then the cell digestion solution was passed through a 40-μm cell sieve. The filtrate was centrifuged at 2000 rpm for 3 min and resuspended in DMEM/F12 complete medium. The second-generation podocytes were cultured on the cell slide. Podocyte characteristic protein (nephrin) was selected to perform cell characterization by immunofluorescence (the samples were sent to Wuhan Servicebio Company).

2.7.2. Cell lines and cell culture

B16F10 cells (mouse melanoma cell line) and L02 cells (human hepatocytes) were maintained in RPMI-1640 medium supplemented with 10 % FBS, 100 U/mL streptomycin, and 100 U/mL penicillin at 37 °C in a humidified atmosphere containing 5 % CO_2.

2.8. Cellular immunofluorescence

B16F10 cells, L02 cells, and primary podocytes were cultured on cell slides for several days. The cells were fixed with 4 % paraformaldehyde at room temperature for 20 min and blocked with 10 % goat serum at 37 °C for 1 h. Then the cells were incubated with rabbit polyclonal antibodies against β3 integrin at 4 °C overnight, and PBS was added as a negative control. Subsequently, the cells were incubated with the secondary antibody (Cy3-conjugated goat anti-rabbit IgG) at 37 °C for 2 h. Then the cell nucleus was stained with DAPI, and an inverted fluorescence microscope (OLYMPUS DP80, Japan) was used to obtain a fluorescence image of the cell.

2.9. Cellular uptake study

2.9.1. RhB-RWrNM fluorescent probe

The inverted fluorescence microscope was used to characterize the specific uptake capacity of the RhB-RWrNM fluorescent probe by primary podocytes. The B16F10 cell line with high expression of αvβ3 integrin was used as a positive control, and the L02 cell line with low expression of αvβ3 integrin was used as a negative control [47]. The cells were seeded into a 12-well plate at an appropriate density. To observe the cell uptake at different time points, cells were incubated with 1 nM RhB-RWrNM fluorescent probe for different durations (1, 2, and 4 h). In the free RWrNM peptide competition inhibition group, the cells were preincubated with 1 mM free RWrNM peptide solution (prepared in culture medium) for 2 h, and then RhB-RWrNM fluorescent probe solution was added, followed by incubation for 4 h. The cells were rinsed with PBS twice and fixed with 4 % paraformaldehyde for 15 min, the cell nucleus was stained with DAPI, and the fluorescence image of the cell was obtained using an inverted fluorescence microscope.

The specific uptake capacity of the RhB-RWrNM fluorescent probe by primary podocytes was quantitatively determined by flow cytometry. The cells were seeded into a 12-well plate or a 60-mm culture dish at an appropriate density, followed by incubation with 1 nM RhB-RWrNM fluorescent probe for 2 h. In the free RWrNM peptide competition inhibition group, cells were preincubated with 1 mM free RWrNM peptide solution for 1 h, and then RhB-RWrNM fluorescent probe solution was added, followed by incubation for 2 h. Subsequently, the cells were resuspended in 300 μL PBS, followed by flow cytometry assay (Cytomics FC500, Beckman Coulter Ltd., USA).

2.9.2. Coumarin 6-loaded 4sPC$_{21}$H$_{21}$C/R

The primary podocytes were seeded into a 12-well cell culture plate at an appropriate density for 5–7 days, followed by incubation with coumarin 6-loaded micelles (5 μg/mL, containing 0.25 μg/mL coumarin 6) for 2 h. In the free coumarin 6 group, the cells were incubated with free coumarin 6 solutions (0.25 μg/mL) for 2 h. After rinsed twice with PBS and fixed with 4 % paraformaldehyde for 15 min, the cell nucleus was stained with DAPI, and the fluorescence image of the cell was obtained with an inverted fluorescence microscope.

The primary podocytes were seeded into a 60-mm cell culture dish at an appropriate density. After treatment according to the above-mentioned experimental method, the cells were digested and resuspended in 300 μL PBS into a single cell suspension for flow cytometry.

2.10. Study on the endocytosis pathways of primary podocytes

The primary podocytes were seeded into a 12-well cell culture plate at an appropriate density for 5–7 days. The cells were preincubated with chlorpromazine hydrochloride (20 μg/mL), M-β-CD (20 mM), amiloride hydrochloride (2 mM), and RWrNM peptide (122 μg/mL) solutions for 30 min, and then the same volume of coumarin 6-loaded micelles (10 μg/mL) were added, followed by incubation for 1 h. After rinsed twice

with PBS and fixed with 4 % paraformaldehyde for 15 min, the cell nucleus was stained with DAPI, and the fluorescence image of the cell was obtained with an inverted fluorescence microscope.

The cells were seeded into a 60-mm cell culture dish at an appropriate density. After treatment according to the above-mentioned experimental method, the cells were digested and resuspended in 300 μL PBS into a single cell suspension for flow cytometry.

2.11. In vitro cytotoxicity assay

The primary podocytes were seeded into a 48-well culture plate at a density of 3×10^4 cells/well for 72 h, the culture medium was replaced with a fresh complete culture medium, and micelles were added to make their concentrations at 5, 10, 50, and 100 μg/mL. There were three replicate wells for each concentration. After incubation for 24 h, the culture medium was replaced by 400 μL MTT solution (0.5 mg/mL, prepared in culture medium), followed by incubation for 4 h. After the supernatant was carefully aspirated, 100 μL DMSO was added into each well, followed by shaking for 10 min in the dark to fully dissolve the crystals. Subsequently, the liquid was transferred into a 96-well plate. The absorbance at 570 nm was measured using a multifunctional microplate reader. The wells without micelles were set as the negative control group. The cell viability was calculated using the formula as follows:

$$\text{Cell viability } (\%) = \frac{A_{sample} - A_{blank}}{A_{control} - A_{blank}} \times 100\%$$

2.12. Hemolysis assay

Blood was obtained from the femoral artery of SD rats to prepare a 2 % (v/v) red blood cell solution. Next, 100 μL Dexac-4sPC$_{21}$H$_{21}$C or Dexac-4sPC$_{21}$H$_{21}$C/R$_2$ micelles at concentrations of 10, 50, 100, 500, and 1000 μg/mL was added into the red blood cell solution. After incubation at 37 °C for 1 h, the mixtures were centrifuged at 3000 rpm for 10 min. Subsequently, 100 μL supernatant was transferred into a 96-well plate. The absorbance at 540 nm was measured using a multifunctional microplate reader. PBS and 1 % Triton X-100-treated red blood cells were set as the negative and positive control groups, respectively. Hemolysis was calculated by the formula as follows:

$$\text{Hemolysis}(\%) = \frac{A_{sample} - A_{negative}}{A_{positive} - A_{negative}} \times 100\%$$

2.13. In vivo evaluation of GFB permeability

Urine samples were collected to determine the amount of polymer nanomaterial that passed through the GFB [30,48]. Briefly, 1200 μg 6-AF conjugated Dexac-4sPC$_{21}$H$_{21}$C, Dexac-4sPC$_{21}$H$_{21}$C/R$_1$, or Dexac-4sPC$_{21}$H$_{21}$C/R$_2$ micelles were injected into the tail vein, and the 24 h urine of five normal SD rats (male, 220–250 g) was collected. The volume of urine was diluted with PBS to 50 mL, and 200 μL diluent was transferred into a 96-well plate, followed by fluorescence determination by a multifunctional microplate reader (Ex/Em = 488/520 nm). The fluorescence average value of the blank group was set as zero.

2.14. In vivo biodistribution

Normal SD rats (male, 220–250 g) were intravenously injected with free DiD or the same dose of DiD-4sPC$_{21}$H$_{21}$C or DiD-4sPC$_{21}$H$_{21}$C/R$_2$ micelles (DiD 50 μg/kg). The rats were sacrificed at predetermined time points (0.5, 1, and 2 h), and organs were collected, including heart, liver, spleen, lung, and kidney. A small animal live imaging system (IVIS Lumina III, PerkinElmer, USA) was used to analyze the fluorescence signal in the collected tissue.

2.15. In vivo colocalization of micelles and glomerular podocytes

Normal SD rats (male, 220–250 g), intravenously injected with DiD-4sPC$_{21}$H$_{21}$C or DiD-4sPC$_{21}$H$_{21}$C/R$_2$ micelles (DiD 100 μg/kg), were sacrificed at 1 h. The kidneys were collected, and paraffin-embedded sections (3 μm) were prepared for immunofluorescence. The podocyte characteristic protein (nephrin) was marked by Alexa Fluor 488-conjugated secondary antibody, and the fluorescence signal of the tissues was assessed with a laser confocal microscope (Zeiss LSM 800, German).

2.16. In vivo pharmacokinetic study

Six normal SD rats (220–250 g, including three males and three females, 300 μg Dexac for each rat) were administered with free Dexac, Dexac-4sPC$_{21}$H$_{21}$C, or Dexac-4sPC$_{21}$H$_{21}$C/R$_2$ micelles by a single intravenous injection. Propylene glycol was used as a solubilizer to prepare the free Dexac solution (1 mg/mL) for intravenous administration. At the designated time points, blood (0.5 mL) was obtained from the orbital vein using a 0.5-mm capillary tube and immediately mixed with heparin (1 %, w/v). The Dex and Dexac concentration in plasma was measured by HPLC. The extraction steps were as follows. The plasma (0.1 mL) was mixed with 0.2 mL of methyltestosterone solution (4 μg/mL) as an internal standard. The mixture was vortex-mixed with 2 mL acetonitrile and 2 mL methanol for 10 min and then centrifuged at 8000 rpm for 10 min. Subsequently, 3 mL supernatant was evaporated to dryness at 37 °C under reduced pressure. Finally, the residue was redissolved in 0.2 mL methanol and filtered with a 0.22-μm nylon filter. The pharmacokinetic parameters were calculated by DAS2.0 (Chinese Professional Committee of Mathematics and Pharmacology, Shanghai, China).

2.17. In vivo safety evaluation

Three normal SD rats (male, 220–250 g) were injected with Dexac-4sPC$_{21}$H$_{21}$C or Dexac-4sPC$_{21}$H$_{21}$C/R$_2$ micelles at a dose of 5 mg per rat for 7 consecutive days. On the 8th day, 1 mL whole blood was obtained from the orbital vein and placed into a 2-mL centrifuge tube at 4 °C. After 1 h, these tubes were centrifuged at 3000 rpm for 15 min, and 0.2 mL of the upper serum was used to measure the levels of ALTL, ASTL, BILT3, CKMB2, CREJ2, LDHI2, UA2, and UREAL by the Cobas c311 biochemical analyzer. The organs (heart, liver, spleen, lung, and kidney) of each group were fixed in 4 % paraformaldehyde for 24 h, then paraffin-embedded sections (3 μm) were prepared, and hematoxylin-eosin (H&E) staining was performed to evaluate the toxicity of the micelles in tissue and organ.

2.18. Data analysis

The results were expressed as mean ± standard deviation, and Graphpad Prism 6.0 (GraphPad Software, USA) was used for analysis and graphic drawing. The Student's t-test was used to evaluate the difference and correlation between the two groups. A one-way analysis of variance (ANOVA) was used to evaluate the significance of multiple comparisons, followed by Tukey-Kramer multiple comparisons. $P < 0.05$ was considered statistically significant (*$P < 0.05$, **$P < 0.01$, ***$P < 0.001$, ****$P < 0.0001$).

3. Results and discussion

3.1. Synthesis and characterization of nanomaterials

As shown in Fig. 1, 4sPCHC/R was synthesized in five steps through ROP and SET LRP polymerizations. Fig. 2 shows the ^{1}H NMR and FTIR spectra. First, in the presence of Sn(Oct)$_2$ as a catalyst, 4sPCL was synthesized by ROP polymerization using pentaerythritol as an initiator. In the ^{1}H NMR spectrum of 4sPCL,δ4.24 corresponded to the methylene

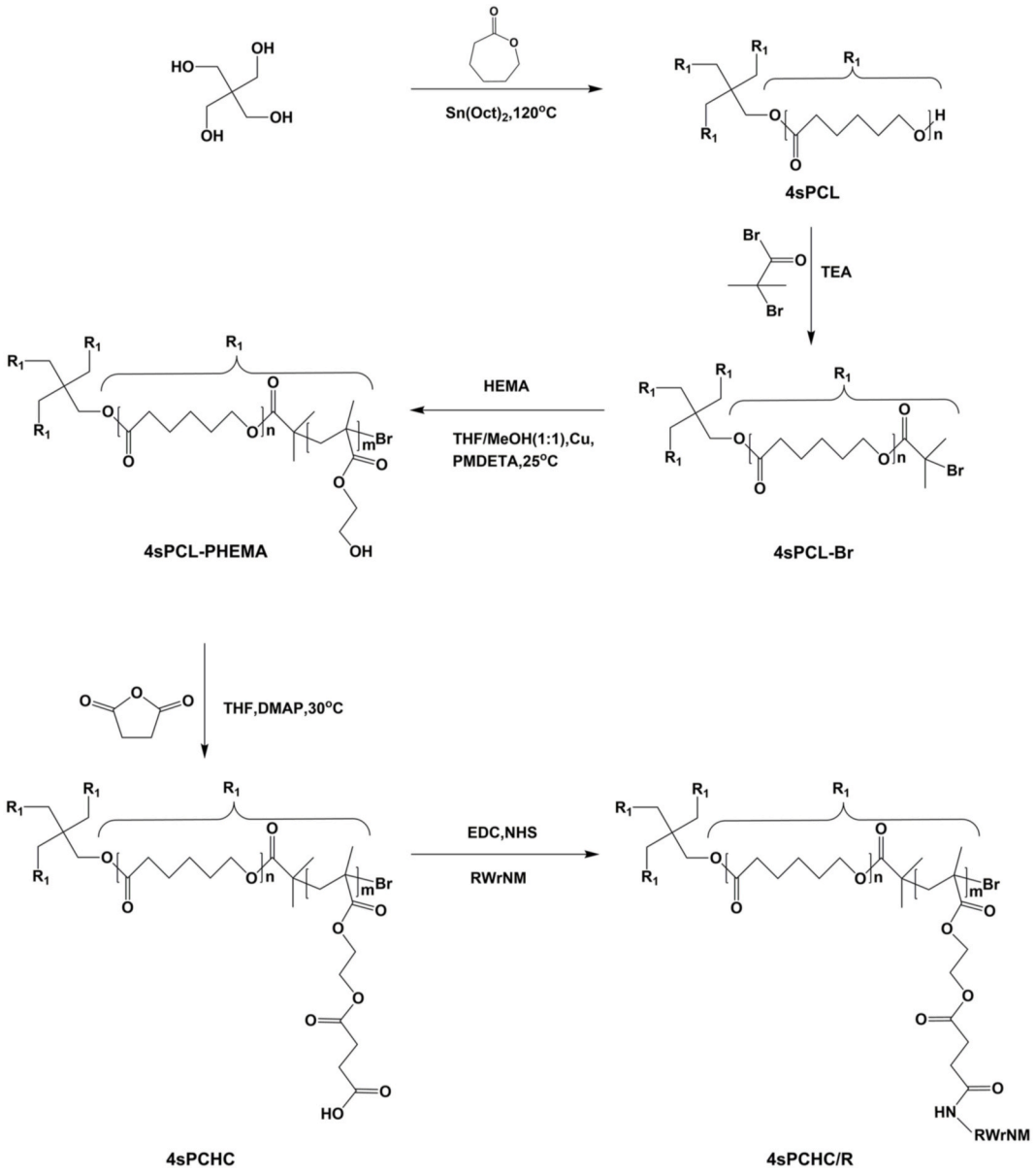

Fig. 1. Synthetic route of 4sPCHC/R.

group adjacent to the caprolactone in pentaerythritol, and the triplet peak at δ3.65 corresponded to the methylene group adjacent to the terminal OH group, confirming the successful synthesis of polycaprolactone by ROP polymerization. The degree of polymerization was calculated by the ratio of the peak areas at δ2.30 and δ3.65. Compared with the FTIR spectra of pentaerythritol and 4sPCL, there was a strong peak at 1721 cm^{-1} in the FTIR spectrum of 4sPCL, which corresponded to the carbonyl peak of the caprolactone unit. The above-mentioned features all indicated the presence of caprolactone units.

Next, the 4sPCL-Br macroinitiator was synthesized through the nucleophilic substitution reaction between the terminal OH groups of 4sPCL and 2-BiBB. Fig. 2A indicates that the triplet peak at δ 3.65 corresponded to the methylene group adjacent to the terminal OH group was shifted to δ 4.17 completely. Meanwhile, there was a new single peak at δ1.93, which corresponded to the methyl group in 2-BiBB attached to the PCL end. The above-mentioned evidence confirmed the successful synthesis of 4sPCL-Br.

Using 4sPCL-Br as the macroinitiator and THF/MeOH (1/1,v/v) as the solvent, the diblock copolymer was synthesized through the SET LRP polymerization. Composition data for 4sPCL-PHEMA polymer is shown in Table 1. The ^{1}H NMR spectrum of 4sPCL-PHEMA at δ3.64 corresponded to the methylene group adjacent to the hydroxyl group of the HEMA unit, confirming the presence of the HEMA unit in the synthesized polymer. The degree of polymerization of HEMA was calculated by analyzing the integral ratio of the peak at δ3.64 (-CH_2**CH_2**OH in the PHEMA block) and the peak at δ1.59 (-$OCOCH_2$**CH_2**CH_2**CH_2**CH_2O- in PCL). In the FTIR spectrum of 4sPCL-PHEMA, the broad peak at 3200–3600 cm^{-1} was attributed to the hydroxyl group in the PHEMA block, which further proved the successful polymerization of HEMA. Besides, the molecular weight of 4sPCL-PHEMA was measured by GPC (HLC-8320GPC, Tosoh Corporation, Japan), as shown in Table S2**.** Except for $4sPCL_{12}PHEMA_{13}$, the other polymers showed good molecular weight polydispersity (less than 2).

After the ring-opening reaction with succinic anhydride, the methylene groups of all HEMA units migrated from δ 3.64 to δ 4.29. This finding indicated that ester bonds were formed between all hydroxyl groups in 4sPCL-PHEMA and succinic anhydride, and the chemical shift of the methylene group in succinic anhydride was overlapped with the methylene group adjacent to the carbonyl structure in the caprolactone unit. Besides, a quantification of the conversion of the HEMA-OH group

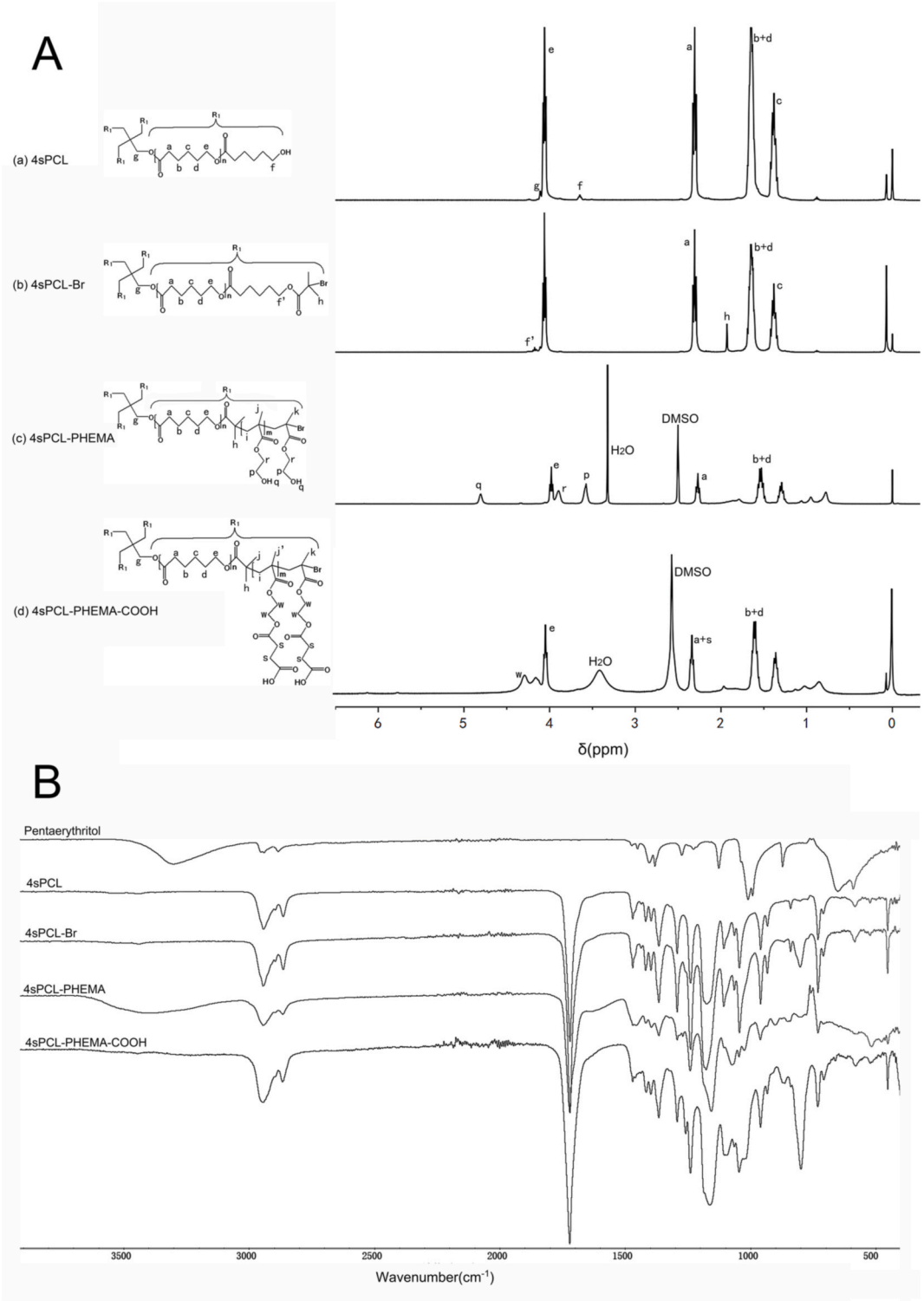

Fig. 2. (A) ^{1}H NMR spectra of 4sPCL in $CDCl_3$, 4sPCL-Br in $CDCl_3$, 4sPCL-PHEMA in DMSO-d_6, 4sPCHC in DMSO-d_6. (B) FTIR spectra of Pentaerythritol, 4sPCL, 4sPCL-Br, 4sPCL-PHEMA, and 4sPCHC.

by reaction with succinic anhydride was measured by potentiometric titration. And the conversion of the HEMA-OH group by reaction with succinic anhydride was 94.1%–97.8 % (Fig. S1). Based on the above-mentioned results, 4sPCHC was successfully synthesized.

Amphiphilic block copolymers can self-assemble into aggregates in selective solvents, and these synthetic amphiphilic star polymers can form micelles in water. The hydrophilic PHEMA-COOH segment modified with succinic anhydride is used as the shell layer of the stable micelles, and the hydrophobic PCL segment constitutes the core. The CMC of amphiphilic copolymers is usually measured by fluorescence technology, with pyrene as the probe [49]. Fig. 3C shows the relationship between the intensity ratio (I337/I334) and the logarithm of the polymer micelle concentration. The CMC of 4sPCHC with different degrees of polymerization measured by the intersection point was 0.40–0.52 μg/mL. The low CMC value indicated that the synthesized polymer had a strong resistance to dilution, thus ensuring stability in

Table 1
Composition data for 4sPCL-based macroinitiators and the resulting 4sPCL-PHEMA polymers.

Initiator (I)	Monomer (M)	M/I	Reaction time(h)	Conversion (%)	Polymer
Pentaerythritol	ε-CL	40/1	24	117.1	$4sPCL_{12}$
Pentaerythritol	ε-CL	80/1	24	105.0	$4sPCL_{21}$
$4sPCL_{12}$-Br	HEMA	60/1	18	86.7	$4sPCL_{12}$-$PHEMA_{13}$
$4sPCL_{12}$-Br	HEMA	100/1	18	96.0	$4sPCL_{12}$-$PHEMA_{24}$
$4sPCL_{21}$-Br	HEMA	92/1	12	91.3	$4sPCL_{21}$-$PHEMA_{21}$
$4sPCL_{21}$-Br	HEMA	172/1	12	97.7	$4sPCL_{21}$-$PHEMA_{42}$

vivo.

We used DLS to determine the particle hydrodynamic diameters and polydispersity index (PDI) of Dexac-4sPCHC with different degrees of polymerization (Figs. 3A and S3). Table 2 shows that the particle hydrodynamic diameter of Dexac-4sPCHC with different degrees of polymerization ranged from 16 to 25 nm, which was compatible with the size of the podocyte filtration slit pore. The images obtained by TEM showed that Dexac-$4sPC_{21}H_{21}C$ and Dexac-$4sPC_{21}H_{21}C/R_2$ could easily form spherical micelles (Fig. 3A-B), and the size was consistent with the results obtained by DLS. Besides, we found the particle size distribution of $4sPC_{21}H_{21}C$ micelles in H_2O was similar to in DMF and THF(Fig. S5), indicating these micelles belong to the unimolecular micelles [50].

We designed a drug-loaded nanocarrier that could pass through the GFB under normal physiological conditions and reach the podocytes as the ultimate goal. We found that Dexac-$4sPC_{12}H_{24}C$ and Dexac-$4sPC_{21}H_{21}C$ micelles had similar ultrasmall particle sizes. Finally, Dexac-$4sPC_{21}H_{21}C$ micelles were chosen to be the best candidate with smaller average particle size and PDI, and its average particle size of 16 nm guaranteed that it could pass through GFB even under normal physiological conditions. However, the limited hydrophilicity of RWrNM peptide probably negatively affected the size of micelles [51]. We designed a single star micelle molecule coupled with 1, 2, and 4 RWrNM peptide molecules for testing. The fluorescence characteristic peaks of tryptophan in RWrNM peptide were scanned by a fluorescence spectrophotometer to characterize the successful coupling of RWrNM peptide and $4sPC_{21}H_{21}C$ (Fig. 3F). Due to the limited hydrophilicity of RWrNM peptides, micelles with higher peptide content had a larger particle size (Table 3 and Fig. S4). We evaluated targeted micelles with different contents of RWrNM peptide by particle size and cellular uptake effect. We finally chose a particle size of targeted micelles less than 24 nm (size compatible with podocyte filtration slit pore) to make sure targeted micelles could smoothly pass through GFB under normal physiological conditions. Thereby, Dexac-$4sPC_{21}H_{21}C/R_2$ micelles were selected to be the suitable targeted micelles to study in further experiments.

To evaluate colloidal stability of micelles in serum, Dexac-$4sPC_{21}H_{21}C$ and Dexac-$4sPC_{21}H_{21}C/R_2$ micelles were fully dispersed in PBS containing 10 % FBS, showing no aggregation behavior within 6 h (Fig. 3D). Besides, Dexac-$4sPC_{21}H_{21}C$ and Dexac-$4sPC_{21}H_{21}C/R_2$ micelles were fully dispersed in PBS containing 50 % FBS, showing less than 2 % leakage of dexamethasone acetate within 4 h (Fig. 3E). It indicated that PHEMA-COOH on the surface of micelles was sufficient to prevent the interaction between micelles and serum proteins.

Because ester bonds in Dexac were prone to hydrolysis and degradation, we first studied the stability of Dexac in H_2O, PBS (pH 7.4), and acetate buffer (pH 4.5). The results showed that 13.3 % of the original drug in PBS (pH 7.4) was indeed degraded within 48 h, while Dexac was stable in H_2O and acetate buffer (pH 4.5) for up to 48 h (Fig. 3G). During the process of micelles phagocytosis in the cell, there will be an acidic environment, such as lysosome [52]. Therefore, it is reasonable to choose acetate buffer (pH 4.5) as an in vitro release medium to simulate in vivo release.

The drug release test was performed under sink conditions in acetate buffer (pH 4.5) at 37 °C. Fig. 3H shows the release behavior of Dexac from micelles. Compared with the free Dexac, micelles had a slower-release effect. All tested micelles reached the Dexac release platform in 24 h.

3.2. αvβ3 integrin expression

We chose αvβ3 integrin as the target receptor because of positive expression in podocytes [41–43]. Besides, they are known to have a high internalization rate, which is important for the delivery of pharmaceutically active substances. In the integrin family, αvβ3 integrin is considered to be very effective for ligand-mediated delivery of nanocarriers to cells [44]. We extracted the kidney tissue from SD suckling rats and inoculated the glomeruli obtained by the sieve method in a culture dish covered with type I collagen. The podocytes were crawled out of the inoculated glomeruli. After 8 days, they were digested, and then purified primary podocytes were obtained using a 40-μm cell sieve. We first confirmed the identity of the podocytes by immunofluorescence characterization of the podocyte characteristic protein (nephrin) (Fig. 4A). Further experiments were carried out to evaluate the actual expressions of αvβ3 integrin receptors in primary podocytes. B16F10 cells with high expression of αvβ3 integrin receptors were used as a positive control, and L02 cells with low expression of αvβ3 integrin receptor were used as a negative control [47]. The immunofluorescence images showed that the αvβ3 integrin receptors were highly expressed in primary podocytes (Fig. 4B).

3.3. Cellular uptake

3.3.1. Evaluation of RWrNM's capacity to target primary podocytes

Fig. 4C shows that compared with L02 cells, a stronger fluorescence signal was observed on the surface of B16F10 cells and primary podocytes. The results indicated that the RhB-RWrNM fluorescent probe had a stronger affinity to B16F10 cells and primary podocytes. Fig. 4D indicates that the uptake of the RhB-RWrNM fluorescent probe by primary podocytes was far more than that of free RhB. After free RWrNM peptide was added to compete for binding to αvβ3 integrin receptors, it was observed that the uptake of the RhB-RWrNM fluorescent probe by primary podocytes was significantly reduced. It indicated that the uptake of RhB-RWrNM fluorescent probe by primary podocytes was specifically mediated by the αvβ3 integrin receptor-ligand interactions.

Further quantitative analysis was performed by flow cytometry (Fig. 4 E-F and S6). Compared with L02 cells, the average fluorescence intensity of B16F10 cells and primary podocytes was significantly higher ($P < 0.001$). Besides, after free RWrNM peptide was added to compete for binding to αvβ3 integrin receptors, the average fluorescence intensity of B16F10 cells and primary podocytes was significantly reduced ($P < 0.0001$), indicating that the uptake of RhB-RWrNM fluorescent probe by B16F10 cells and primary podocytes was specifically mediated by the αvβ3 integrin receptor-ligand interactions.

The affinity of RWrNM peptide to B16F10 cells, primary podocytes, and L02 cells was evaluated by the ratio of the average fluorescence intensity between RhB-RWrNM fluorescent probe and free RhB (Fig. 4G). In B16F10 cells, the fluorescence intensity of RhB-RWrNM fluorescent probe was 24.4 ± 1.2 times higher compared with the free RhB. In primary podocytes, the fluorescence intensity of RhB-RWrNM fluorescent probe was 24.9 ± 1.7 times higher compared with the free RhB. In L02 cells, the fluorescence intensity of RhB-RWrNM fluorescent probe was 4.4 ± 0.5 times higher compared with the free RhB. The results showed that RWrNM peptide had a very high affinity to B16F10 cells and primary podocytes, and a low affinity to L02 cells.

Therefore, the RWrNM peptide had an efficient ability to target αvβ3 integrin receptors on the surface of primary podocytes. Moreover, in

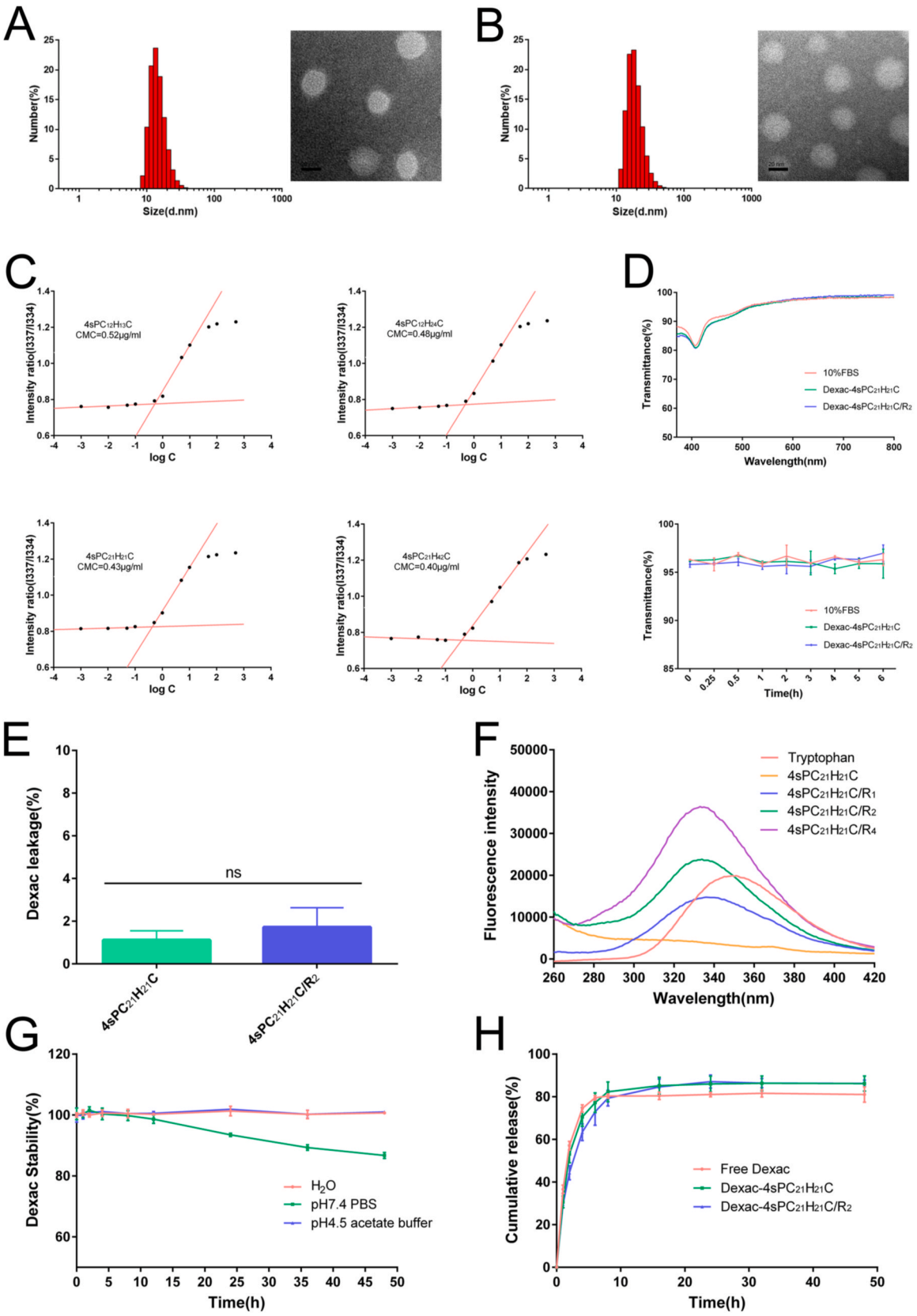

Fig. 3. (A) The particle size distribution of Dexac-4sPC$_{21}$H$_{21}$C micelles was measured by DLS and TEM. scale bar, 20 nm. (B) The particle size distribution of Dexac-4sPC$_{21}$H$_{21}$C/R$_2$ micelles was measured by DLS and TEM. scale bar, 20 nm. (C) The plots of intensity ratio (I337/I334) vs logarithm of 4sPCHC with different degrees of polymerization. (D) Light transmittance evaluation of serum colloidal stability. (n = 3) (E) Leakage of Dexac from Dexac-4sPC$_{21}$H$_{21}$C and Dexac-4sPC$_{21}$H$_{21}$C/R$_2$ micelles in 50 % FBS.(n = 3) (F) Tryptophan fluorescence scanning curve of 4sPC$_{21}$H$_{21}$C/R micelles with different RWrNM peptide contents. (G) Stability of Dexac in water, PBS (pH 7.4), and acetate buffer (pH 4.5). (n = 3) (H) In vitro release curve of Dexac-loaded micelles in acetate buffer (pH 4.5). (n = 3).

Table 2
Particle size, PDI, zeta potential, CMC, EE, and DLC of Dexac-4sPCHC (n = 3).

Polymer	Size (nm)	PDI	Zeta Potential (mV)	EE(%)	DL(%)	CMC (μg/ml)
$4sPC_{12}H_{13}C$	25.1 ± 1.8	0.09 ± 0.03	−25.9 ± 1.6	34.0 ± 2.2	3.29 ± 0.16	0.52
$4sPC_{12}H_{24}C$	17.0 ± 1.1	0.17 ± 0.01	−30.4 ± 2.1	34.9 ± 2.7	3.37 ± 0.21	0.48
$4sPC_{21}H_{21}C$	16.0 ± 0.9	0.15 ± 0.02	−30.6 ± 1.6	33.5 ± 2.3	3.24 ± 0.17	0.43
$4sPC_{21}H_{42}C$	20.8 ± 2.0	0.21 ± 0.01	−29.1 ± 0.7	31.4 ± 1.3	3.04 ± 0.10	0.40

Table 3
Particle size, PDI, zeta potential, EE, and DLC of Dexac-4sPCHC/R (n = 3).

Polymer	RWrNM amount	Size (nm)	PDI	Zeta Potential (mV)	EE (%)	DL(%)
$4sPC_{21}H_{21}C/R_1$	1	18.4 ± 0.8	0.27 ± 0.01	−32.9 ± 2.4	33.4 ± 2.3	3.23 ± 0.18
$4sPC_{21}H_{21}C/R_2$	2	20.3 ± 0.9	0.24 ± 0.01	−29.5 ± 4.9	33.0 ± 3.3	3.19 ± 0.25
$4sPC_{21}H_{21}C/R_4$	4	30.5 ± 3.1	0.21 ± 0.01	−28.3 ± 3.2	32.8 ± 3.1	3.17 ± 0.24

B16F10 cells and primary podocytes, the ratio of average fluorescence intensity between RhB-RWrNM fluorescent probe and free RhB was not statistically different ($P > 0.05$). It indicated that the targeted effect of RWrNM peptide to primary podocytes was comparable to that of B16F10 cells.

3.3.2. The specific uptake of $4sPC_{21}H_{21}C/R$ micelles with different RWrNM contents by primary podocytes

Fig. 5A shows that compared with free coumarin 6, the micelles groups had obvious stronger fluorescence signal, indicating that micelles could significantly increase the uptake of coumarin 6 in primary podocytes. As the content of RWrNM peptide in micelles was increased, the amount of fluorescence signal was also enhanced. The results indicated that RWrNM peptides could increase the uptake of targeted micelles through receptor-ligand-mediated interactions in primary podocytes.

Further quantitative analysis was performed by flow cytometry (Fig. 5B-C). Compared with $4sPC_{21}H_{21}C$, $4sPC_{21}H_{21}C/R_1$ (1.09 ± 0.02 times), $4sPC_{21}H_{21}C/R_2$ (1.84 ± 0.01 times) and $4sPC_{21}H_{21}C/R_4$ (2.28 ± 0.02 times) micelles had higher uptake ($P < 0.01$). The results indicated that $4sPC_{21}H_{21}C/R$ micelles could increase the uptake of coumarin 6 in primary podocytes through receptor-ligand-mediated interactions, and the targeted effect of RWrNM peptide to primary podocytes was quite significant.

3.4. Study on the endocytosis pathways of primary podocytes

An endocytosis inhibition experiment was performed to verify how $4sPC_{21}H_{21}C$ and $4sPC_{21}H_{21}C/R_2$ micelles were delivered to podocytes (Fig. 6A–C and S7). To explore the effect of temperature on cellular uptake, primary podocytes were incubated at 37 °C and 4 °C, respectively. When the temperature was changed from 37 °C to 4 °C, the uptake rate decreased by nearly 75 % ($P < 0.0001$), indicating that the uptake of $4sPC_{21}H_{21}C$ and $4sPC_{21}H_{21}C/R_2$ micelles depended on energy [53]. Chlorpromazine, an inhibitor of clathrin-dependent endocytosis [54], slightly prevented the uptake of $4sPC_{21}H_{21}C$ and $4sPC_{21}H_{21}C/R_2$ micelles ($P < 0.001$). M-β-CD, an inhibitor of caveolae-mediated endocytosis [55], decreased the uptake rate by nearly 90 % ($P < 0.0001$), which greatly prevented the uptake of $4sPC_{21}H_{21}C$ and $4sPC_{21}H_{21}C/R_2$ micelles. Amiloride, an inhibitor of the effect of macropinocytosis [56], did not decrease the uptake of $4sPC_{21}H_{21}C$ and $4sPC_{21}H_{21}C/R_2$ micelles. The results indicated that the endocytosis was mainly mediated by the caveolae, and the clathrin-dependent endocytosis was an auxiliary pathway to participate in the endocytosis of $4sPC_{21}H_{21}C$ and $4sPC_{21}H_{21}C/R_2$ micelles in primary podocytes. After pretreatment with free RWrNM peptide, the uptake of $4sPC_{21}H_{21}C$ and $4sPC_{21}H_{21}C/R_2$ micelles was decreased by 3.57 % ($P > 0.05$) and 14.69 % ($P < 0.001$), respectively, compared with the control group. Receptor competition studies showed that the cellular uptake of $4sPC_{21}H_{21}C/R_2$ micelles was partly mediated by the αvβ3 integrin receptor on the podocyte membrane.

3.5. In vitro cytotoxicity assay

When incubated with free Dexac and Dexac-$4sPC_{21}H_{21}C/R_2$ micelles, the viability of the primary podocytes was not affected even at the highest concentration, indicating that Dexac-$4sPC_{21}H_{21}C/R_2$ micelles had excellent cell safety (Fig. 6D-E). At a concentration of 50 μg/mL, Dexac-$4sPC_{21}H_{21}C$ micelles decreased the viability of primary podocytes to 78 %, which might be attributed to the abundant carboxyl groups on the surface of $4sPC_{21}H_{21}C$ micelles with a large number of negative charges, leading to cell apoptosis [57].

3.6. Hemolysis assay

Hemolysis of less than 20 % has been always considered non-toxic [58]. The hemolysis analysis of Dexac-$4sPC_{21}H_{21}C$ and Dexac-$4sPC_{21}H_{21}C/R_2$ micelles showed that hemoglobin release was not increased significantly, it did not show a concentration-dependent pattern in hemolysis, and all the hemolysis rates were less than 5 % (Fig. 6F). Since Dexac-$4sPC_{21}H_{21}C$ and Dexac-$4sPC_{21}H_{21}C/R_2$ micelles had negative potentials at pH 7.4, the negative charges on their surfaces were repelled by the negatively charged membranes of red blood cells, making them unable to interact with the negatively charged membranes of red blood cells. It indicated that Dexac-$4sPC_{21}H_{21}C$ and Dexac-$4sPC_{21}H_{21}C/R_2$ micelles had good biosecurity.

3.7. In vivo evaluation of GFB permeability

In normal SD rats, the permeability of 6-AF conjugated Dexac-$4sPC_{21}H_{21}C$, Dexac-$4sPC_{21}H_{21}C/R_1$, and Dexac-$4sPC_{21}H_{21}C/R_2$ micelles in 24-h urine were 50.4 ± 6.6 %, 48.7 ± 10.1 %, and 60.0 ± 2.6 %, respectively (Figs. 6G and S8). There was no significant difference in the results of the one-way analysis of variance ($P > 0.05$). The reason for high GFB permeability was probably attributed to that the particle size difference in Dexac-$4sPC_{21}H_{21}C$, Dexac-$4sPC_{21}H_{21}C/R_1$, and Dexac-$4sPC_{21}H_{21}C/R_2$ micelles were very small, and the particle size was smaller than the average diameter of the podocyte foot process slit hole (24 nm) [33–38]. The results showed that Dexac-$4sPC_{21}H_{21}C/R_2$ micelles still had high GFB permeability even there was no damage to GFB, suggesting that Dexac-$4sPC_{21}H_{21}C/R_2$ micelles could not only cure GFB to reduce urine protein levels in severe podocyte damage, but also hopefully play a therapeutic role in the early stage of podocyte damage. Thereby, Dexac-$4sPC_{21}H_{21}C/R_2$ micelles were confirmed to be the best-targeted micelles to study in further experiments.

3.8. In vivo biodistribution

Due to the low drug delivery efficiency, many nano-scale drugs have poor therapeutic effects in vivo [59]. To observe how $4sPC_{21}H_{21}C/R_2$ micelles were distributed in normal SD rats, DiD-loaded micelles were used (Fig. 7A–C and S9). In vivo fluorescence images showed that micelles could deliver more DiD to the kidney compared with the free DiD. Moreover, in vivo fluorescence images showed that $4sPC_{21}H_{21}C/R_2$

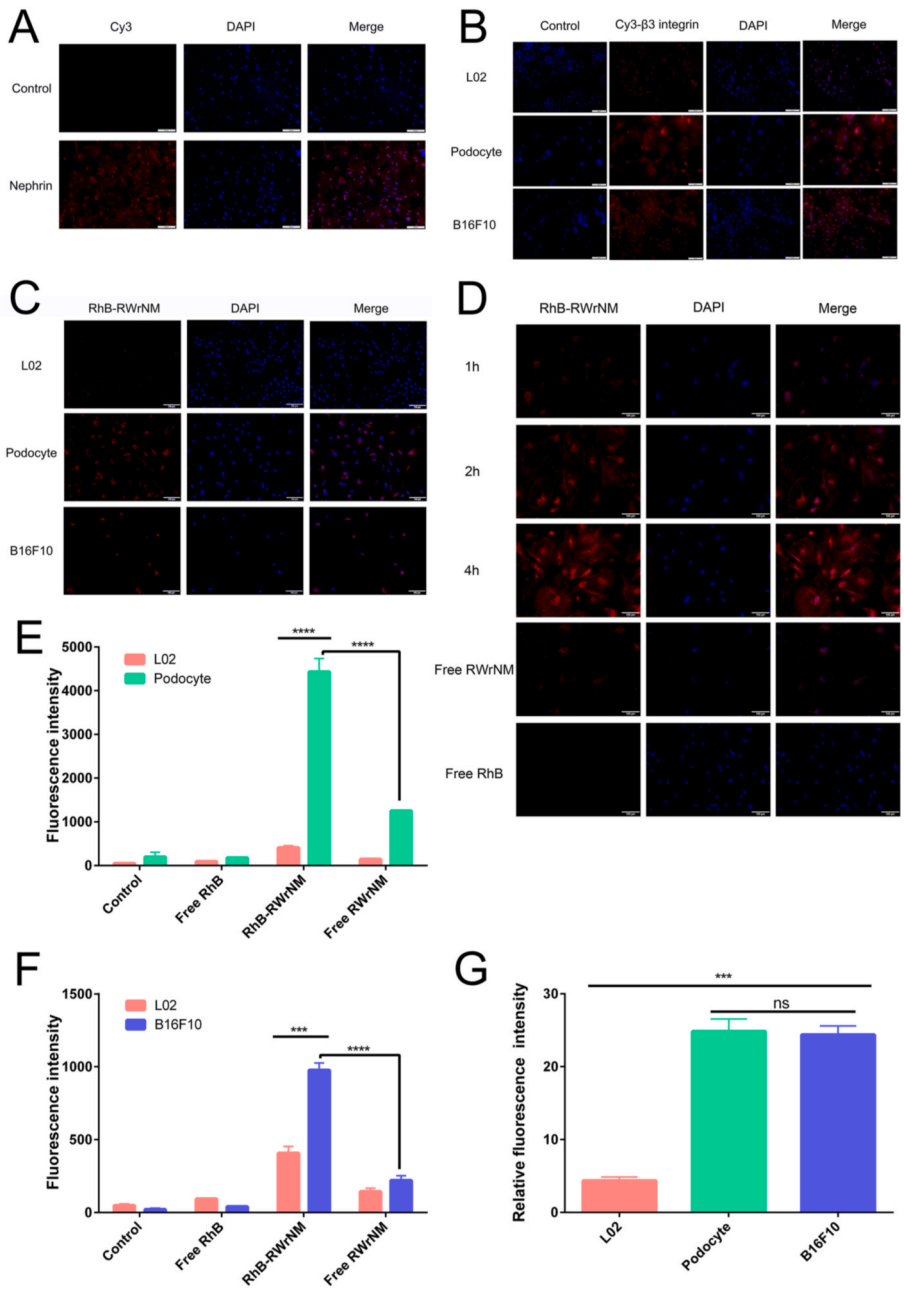

Fig. 4. (A) Immunofluorescence images of nephrin expression in primary podocytes.scale bar, 200 μm. (B) Immunofluorescence images of αvβ3 integrin receptor expression in primary podocytes. B16F10 cells were used as a positive control for αvβ3 integrin receptor expression, and L02 cells were used as a negative control for αvβ3 integrin receptor expression. The results showed that the high expression of αvβ3 integrin receptors was observed in primary podocytes. scale bar, 100 μm. (C) Inverted fluorescence microscopy was used to characterize the specific uptake of RhB-RWrNM fluorescent probes by primary podocytes through αvβ3 integrin receptors. scale bar, 100 μm. (D) An inverted fluorescence microscope was used to characterize the specific uptake of RhB-RWrNM fluorescent probes by primary podocytes. Both free RWrNM peptide and free RhB were incubated with primary podocytes for 4 h. scale bar, 100 μm. (E) Flow cytometry was used for the quantitative determination of the affinity of RWrNM peptide to αvβ3 integrin receptor compared with primary podocytes and L02 cells. (n = 3) (F) Comparison of B16F10 cells and L02 cells. (n = 3) (G) Comparison of the affinity of RWrNM peptide to B16F10 cells, primary podocytes, and L02 cells together by the ratio of average fluorescence intensity between RhB-RWrNM fluorescent probe and free RhB. (n = 3).

micelles had a stronger renal accumulation capacity compared with $4sPC_{21}H_{21}C$ micelles (Figs. 7B and S9C). In the semiquantitative data, compared to the mean value of average radiant efficiency, $4sPC_{21}H_{21}C/R_2$ micelles was always higher than $4sPC_{21}H_{21}C$ micelles after 1h, while $4sPC_{21}H_{21}C/R_2$ micelles was a little lower than $4sPC_{21}H_{21}C$ at 0.5h, indicated that $4sPC_{21}H_{21}C$ micelles reached kidney earlier than $4sPC_{21}H_{21}C/R_2$ micelles (Figs. 7C and S9D). It is well known that the biodistribution of nanocarriers is easily affected by their surface ligands, charge, shape, and size [29,60,61]. Because $4sPC_{21}H_{21}C$ micelles had a smaller particle size and were easier to pass through GFB, they could reach the urine space earlier to interact with podocytes. However, these passively accumulated micelles were quickly transferred to the bladder with urine, resulting in the short contact time between micelles and podocytes, and the accumulation of micelles was gradually decreased with time. Although $4sPC_{21}H_{21}C/R_2$ micelles reached the kidney slightly slower, the presence of αvβ3 integrin ligand RWrNM peptide increased the receptor-ligand-mediated interaction between micelles and podocytes, and its kidney accumulation capacity was higher. Besides, as shown in Fig. 7D–F, the urinary excretion curve of DiD-$4sPC_{21}H_{21}C$ and DiD-$4sPC_{21}H_{21}C/R_2$ micelles also proved that $4sPC_{21}H_{21}C$ reached urine faster and $4sPC_{21}H_{21}C/R_2$ micelles were retained in the glomerulus and hence reached urine in a delayed manner. Moreover, in the early time(0–12h), $4sPC_{21}H_{21}C$ excreted more than $4sPC_{21}H_{21}C/R_2$, but $4sPC_{21}H_{21}C/R_2$ excreted more than $4sPC_{21}H_{21}C$ in later time(12–24h).

3.9. *In vivo colocalization of micelles and glomerular podocytes*

To better confirm whether $4sPC_{21}H_{21}C$ and $4sPC_{21}H_{21}C/R_2$ micelles could pass through GFB and accumulate in podocytes, the kidneys were sliced into thin slices(3 μm) and subjected to further immunofluorescence analysis (Fig. 7 G-H and S10). In this experiment, the podocyte characteristic protein (nephrin) was marked by the Alexa Fluor 488 conjugated secondary antibody. The fluorescence images showed that

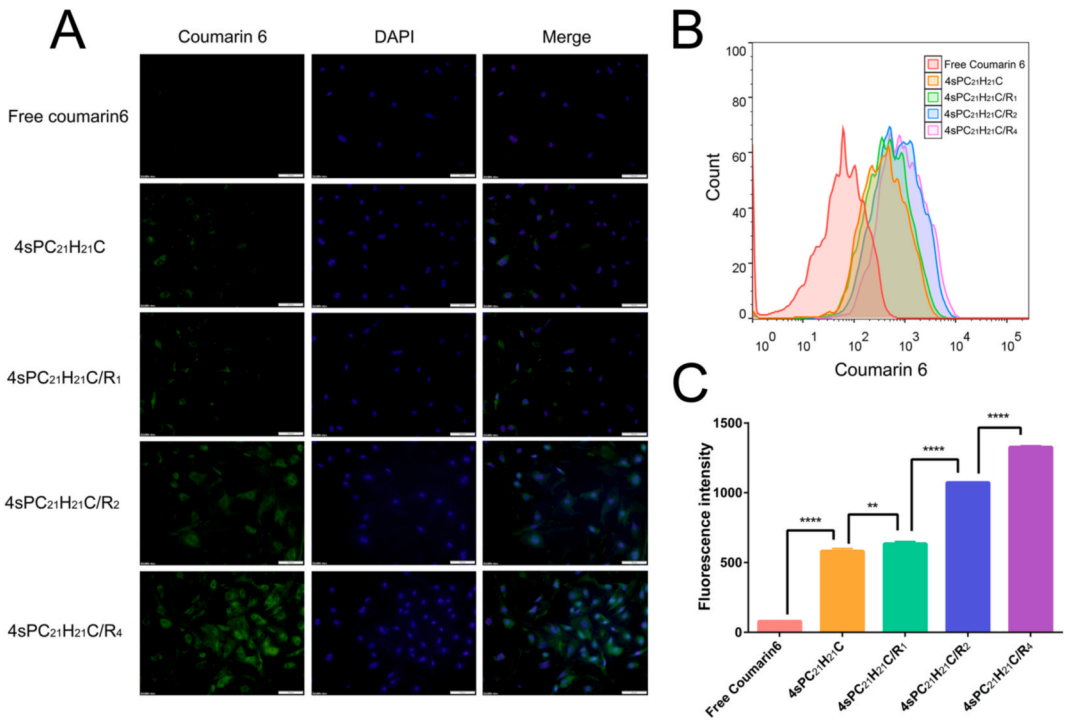

Fig. 5. (A) Fluorescence image of coumarin 6-loaded 4sPC$_{21}$H$_{21}$C/R micelles in primary podocytes. scale bar, 100 μm. (B–C) Flow cytometry was used for the quantitative determination of the uptake of coumarin 6-loaded 4sPC$_{21}$H$_{21}$C/R micelles in primary podocytes. (n = 3).

the DiD-4sPC$_{21}$H$_{21}$C or DiD-4sPC$_{21}$H$_{21}$C/R$_2$ micelles (red) and the podocyte characteristic protein (nephrin, green) were strongly overlapped (Fig. 7G). And the value of Pearson's correlation coefficient was more than 0.9, indicated that both 4sPC$_{21}$H$_{21}$C and 4sPC$_{21}$H$_{21}$C/R$_2$ had a strong colocalization degree with glomerular podocytes (Fig. 7H). Those results further confirmed that 4sPC$_{21}$H$_{21}$C and 4sPC$_{21}$H$_{21}$C/R$_2$ micelles could pass through GFB smoothly and accumulate in podocytes. Moreover, the DiD gray value of DiD-4sPC$_{21}$H$_{21}$C/R$_2$ micelles was higher compared with DiD-4sPC$_{21}$H$_{21}$C micelles($P < 0.05$) (Fig. S10A). It indicated that podocytes had a higher uptake effect of 4sPC$_{21}$H$_{21}$C/R$_2$ micelles in vivo, which was consistent with the results of cellular experiments in vitro.

3.10. In vivo pharmacokinetic study

In recent years, the research on the targeted podocyte drug delivery system is extremely lacking in pharmacokinetic research data. However, the pharmacokinetic parameters show great impacts on the circulation of drug-loaded nanocarriers in vivo [62]. After a single intravenous injection of 300 μg free Dexac, or the same dose of Dexac-4sPC$_{21}$H$_{21}$C, and Dexac-4sPC$_{21}$H$_{21}$C/R$_2$ micelles in normal SD rats, Dexac was quickly converted into Dex in vivo, and a total of Dex (both Dex and Dexac) in plasma were determined by HPLC. Fig. 8A illustrates the concentration-time curve of plasma total Dex. Fig. 8B–C, S11, and Table S4 display the pharmacokinetic parameters involving the plasma elimination half-life (t1/2), mean residence time [MRT$_{(0-\infty)}$], and area under the curve [AUC$_{(0-\infty)}$] of Dexac of different formulations. The results showed that Dexac-4sPC$_{21}$H$_{21}$C and Dexac-4sPC$_{21}$H$_{21}$C/R$_2$ micelles decreased the t1/2 of Dexac from 3.24 ± 0.47 h to 1.62 ± 0.23 h and 2.09 ± 0.18 h, respectively ($P < 0.0001$). Dexac-4sPC$_{21}$H$_{21}$C and Dexac-4sPC$_{21}$H$_{21}$C/R$_2$ micelles also decreased the MRT$_{(0-\infty)}$ of Dexac from 3.88 ± 0.72 h to 1.94 ± 0.30 h and 2.40 ± 0.25 h, respectively ($P < 0.001$). It indicated that a large amount of Dexac-4sPC$_{21}$H$_{21}$C and Dexac-4sPC$_{21}$H$_{21}$C/R$_2$ micelles carried drugs passed through the GFB and reached podocytes, resulting in a decrease in the t1/2 and MRT$_{(0-\infty)}$ of Dexac. This result was consistent with the high GFB permeability.

3.11. In vivo safety evaluation

To evaluate the safety of the micelles, the heart, liver, spleen, lung, and kidney were histopathologically evaluated (Fig. 8D). These organs showed no signs of cell or tissue damage after continuous injection for 7 days, and there was no significant difference between the micelles group and the normal group. Roche cobas311 biochemical analyzer was used to further quantitatively evaluate the levels of ALTL, ASTL, BILT3, CKMB2, CREJ2, LDHI2, UA2, and UREAL in serum (Fig. 8E). After one-way analysis of variance, there was no significant difference in the index of heart, liver, and kidney between the normal group and Dexac-4sPC$_{21}$H$_{21}$C/R$_2$ micelles group ($P > 0.05$), indicating that Dexac-4sPC$_{21}$H$_{21}$C/R$_2$ micelles could be a safe carrier for treatment research in the future.

In many kidney diseases, the GFB is broken and can become more permeable [30,39,40]. Therefore, we expected that Dexac-4sPC$_{21}$H$_{21}$C/R$_2$ micelles might further accumulate in glomerular podocytes in CKD patients. In general, our newly designed nano-micelle platform had the potential as a targeted drug delivery carrier for kidney applications.

4. Conclusions

In this study, we synthesized four-arm star polymers conjugated with a novel linear RWrNM peptide. 4sPCL-PHEMA polymers with different degrees of polymerization were synthesized by ROP and SET LRP polymerization, and after modification with succinic anhydride, polymers were coupled with linear RWrNM peptide to form ultrasmall drug-loaded micelles with a size of 16–30 nm. The novel linear RWrNM peptide-conjugated micelles showed a high affinity to primary podocytes comparable to B16F10 cells. The biodistribution experiment in normal SD rats verified its high targeted effect on the kidney and excellent podocyte colocalization effect. Even under normal physiological conditions, it still possessed high GFB permeability, and the plasma elimination half-life of Dexac was decreased to 1.62–2.09h, which was consistent with the high GFB permeability. Moreover, the in vitro and in

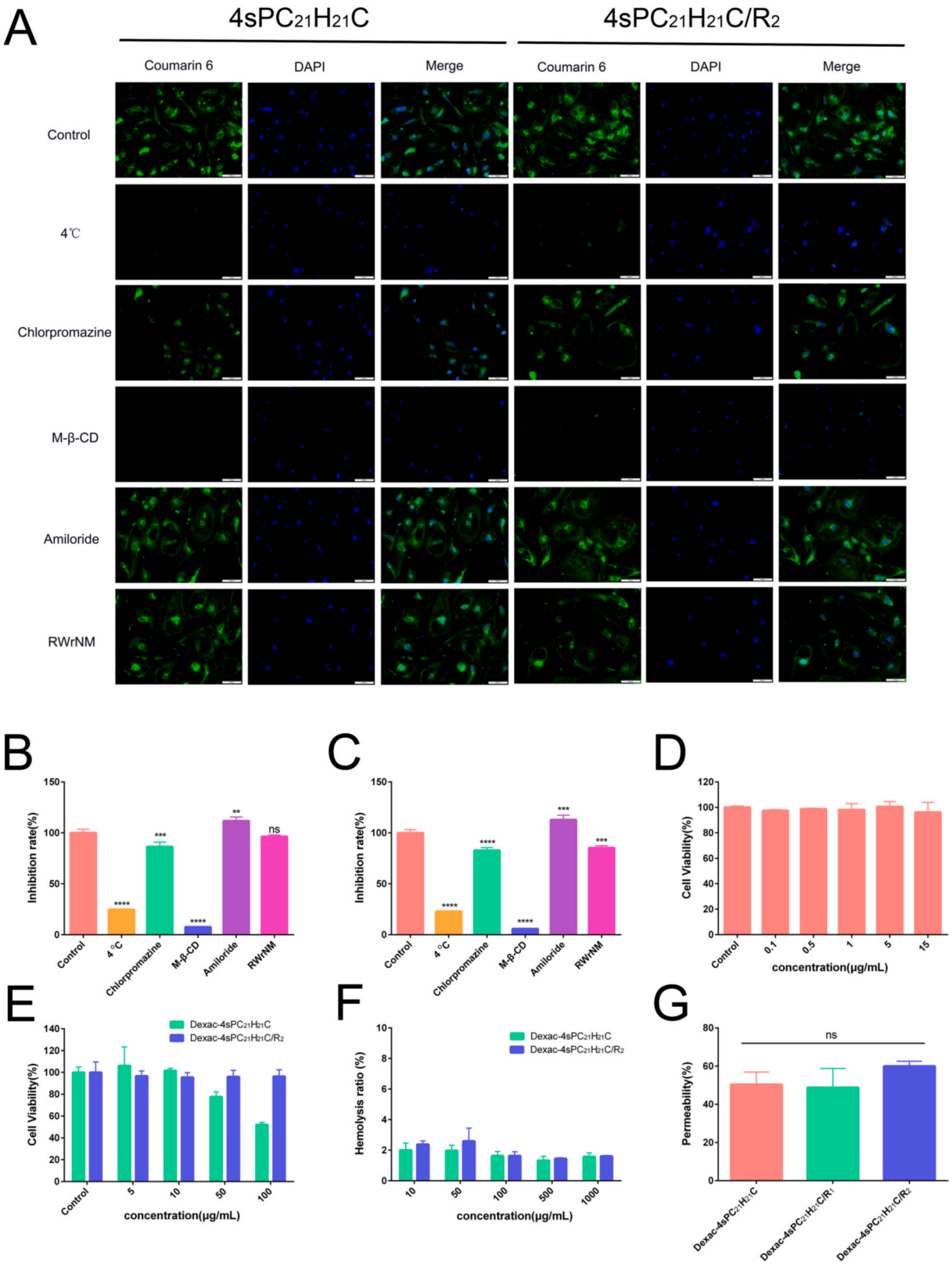

Fig. 6. (A) Images of the endocytosis inhibition assay of the coumarin 6-loaded 4sPC$_{21}$H$_{21}$C and 4sPC$_{21}$H$_{21}$C/R micelles on primary podocytes. scale bar, 100 μm (B) Flow cytometry for the quantitative determination of the endocytosis inhibition rate of the coumarin 6-loaded 4sPC$_{21}$H$_{21}$C micelles with different inhibitors on primary podocytes. (n = 3) (C) Flow cytometry for the quantitative determination of the endocytosis inhibition rate of the coumarin 6-loaded 4sPC$_{21}$H$_{21}$C/R$_2$ micelles with different inhibitors in primary podocytes. (n = 3) (D) Toxicity determination of free Dexac on primary podocytes. (n = 3) (E) Toxicity determination of Dexac-4sPC$_{21}$H$_{21}$C and Dexac-4sPC$_{21}$H$_{21}$C/R$_2$ micelles on primary podocytes. (n = 3). (F) Hemolysis determination of Dexac-4sPC$_{21}$H$_{21}$C and Dexac-4sPC$_{21}$H$_{21}$C/R$_2$ micelles. (n = 3). (G) GFB permeability determination of Dexac-4sPC$_{21}$H$_{21}$C, Dexac-4sPC$_{21}$H$_{21}$C/R$_1$, and Dexac-4sPC$_{21}$H$_{21}$C/R$_2$ micelles in normal SD rats. (n = 5).

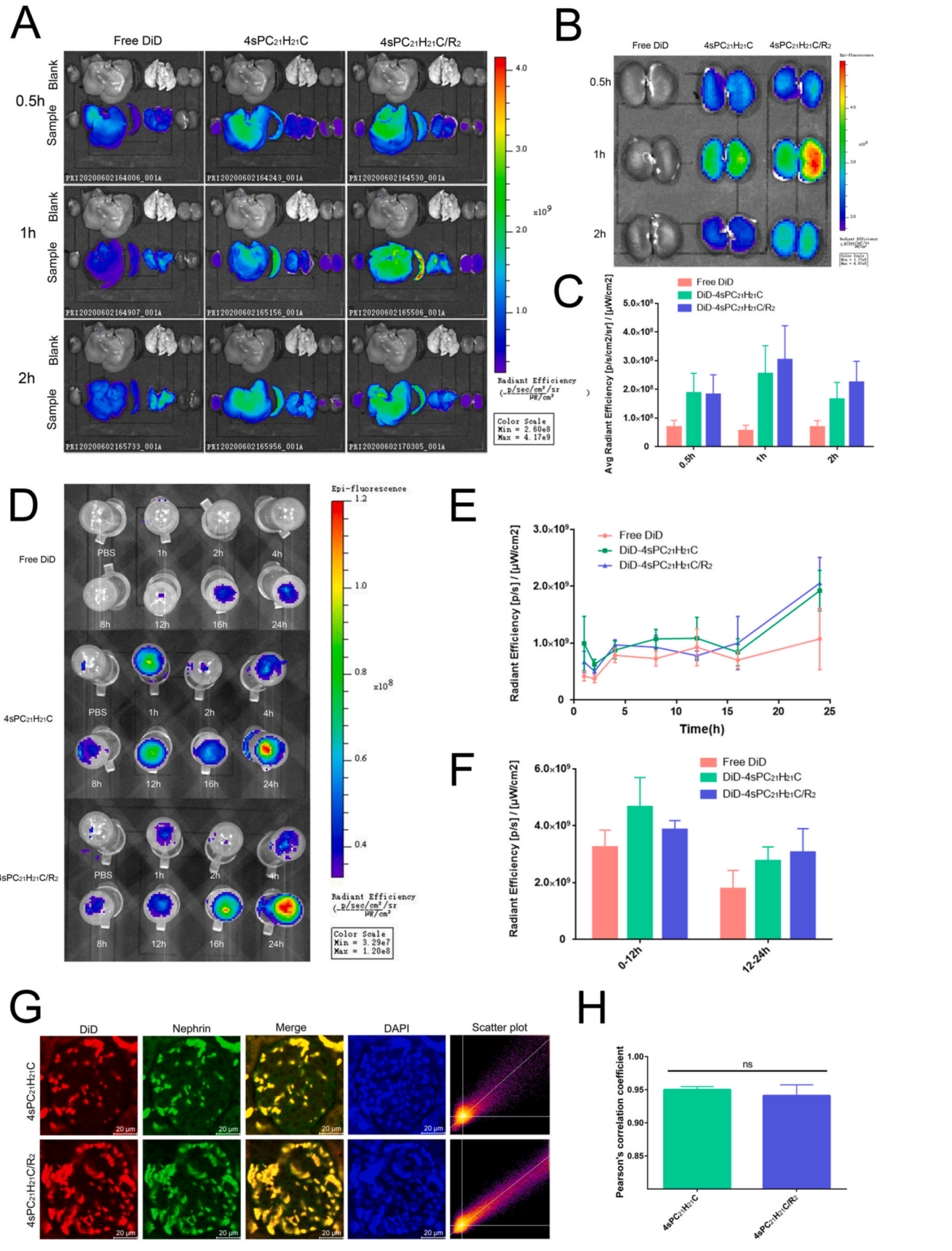

(caption on next page)

Fig. 7. (A) Fluorescence images of DiD-4sPC$_{21}$H$_{21}$C and DiD-4sPC$_{21}$H$_{21}$C/R$_2$ micelles in the isolated organs of normal SD rats. (B) Fluorescence images of DiD-4sPC$_{21}$H$_{21}$C and DiD-4sPC$_{21}$H$_{21}$C/R$_2$ micelles in the isolated kidneys of normal SD rats. (C) The average radiant efficiency of DiD-4sPC$_{21}$H$_{21}$C and DiD-4sPC$_{21}$H$_{21}$C/R$_2$ micelles in the isolated kidneys of normal SD rats. (D) Fluorescence images of free DiD, DiD-4sPC$_{21}$H$_{21}$C and DiD-4sPC$_{21}$H$_{21}$C/R$_2$ micelles in the urine of 0–1,1–2,2-4,4–8,8-12,12–16, and 16–24h.(E)The urinary excretion curve of free DiD, DiD-4sPC$_{21}$H$_{21}$C and DiD-4sPC$_{21}$H$_{21}$C/R$_2$ micelles in the urine.(n = 3).(F) The total radiant efficiency of free DiD, DiD-4sPC$_{21}$H$_{21}$C, and DiD-4sPC$_{21}$H$_{21}$C/R$_2$ micelles in the urine of 0–12h and 12–24h. (n = 3). (G) Colocalization fluorescence images of DiD-4sPC$_{21}$H$_{21}$C, DiD-4sPC$_{21}$H$_{21}$C/R$_2$ micelles (red), and Alexa Fluor 488-marked the podocyte characteristic protein (nephrin, green). scale bar, 20 μm. (H) Colocalization degree was evaluated by Pearson's correlation coefficient. (n = 3). (For interpretation of the references to colour in this figure legend, the reader is referred to the Web version of this article.)

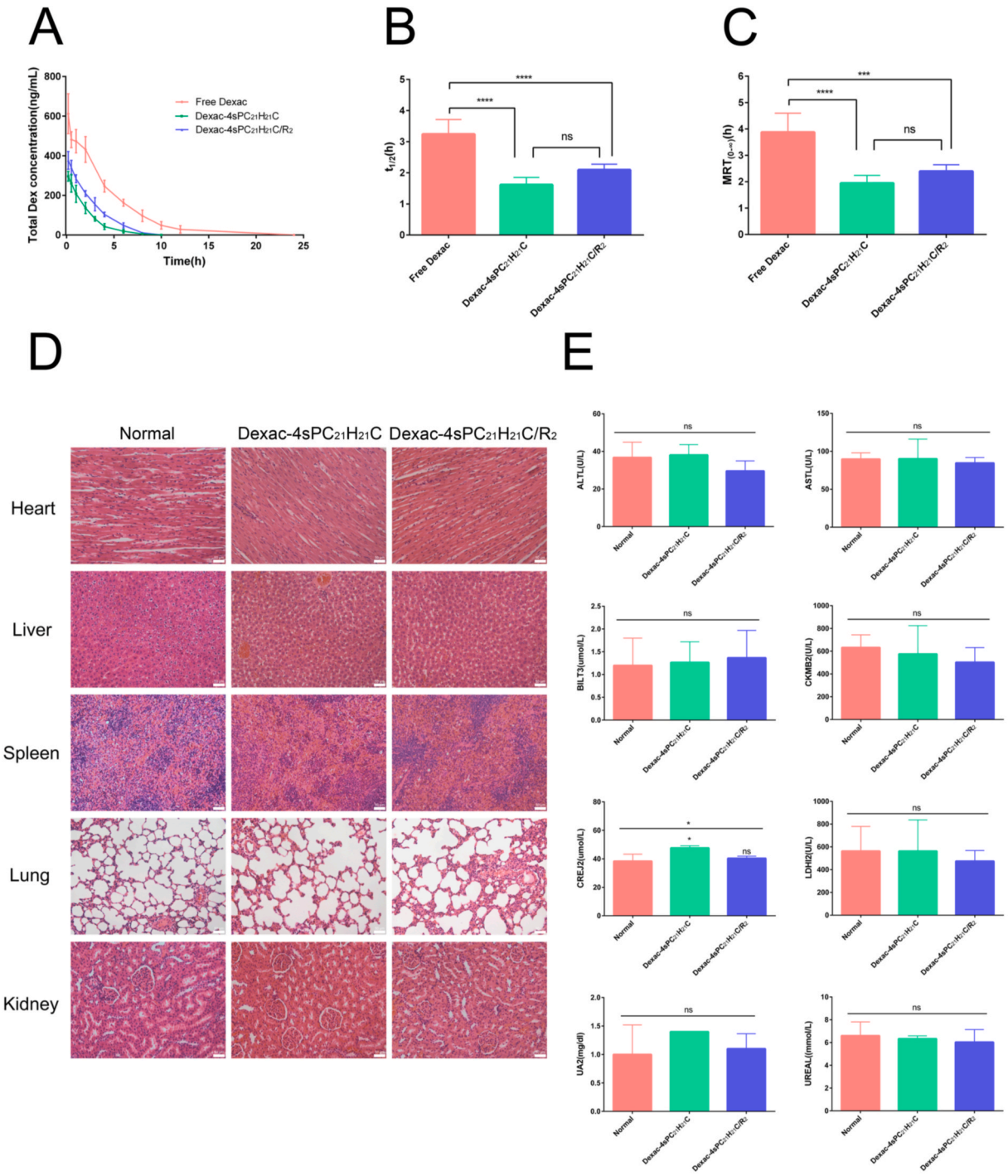

Fig. 8. (A) The plasma total Dex concentration curve of free Dexac, Dexac-4sPC$_{21}$H$_{21}$C, and Dexac-4sPC$_{21}$H$_{21}$C/R$_2$ micelles in normal SD rats. (n = 6) (B–C) The plasma Dexac elimination half-life (t1/2) and Mean Residence Time (MRT) of free Dexac, Dexac-4sPC$_{21}$H$_{21}$C, and Dexac-4sPC$_{21}$H$_{21}$C/R$_2$ micelles in normal SD rats. (n = 6) (D) Heart, liver, spleen, lung, and kidney of SD rats stained with H&E after tail vein injection of Dexac-4sPC$_{21}$H$_{21}$C, or Dexac-4sPC$_{21}$H$_{21}$C/R$_2$ micelles for 7 days. All organs showed normal morphology. Scale bar, 50 μm. (E) After intravenous injection of Dexac-4sPC$_{21}$H$_{21}$C and Dexac-4sPC$_{21}$H$_{21}$C/R$_2$ micelles into the tail vein for 7 days, the levels of ALTL, ASTL, BILT3, CKMB2, CREJ2, LDHI2, UA2, and UREAL in serum were measured by the Cobas c311 biochemical analyzer. (n = 3).

vivo excellent safety reduced the side effects of Dexac. The results of the study indicated that this novel ultrasmall drug-loaded micelles could be used as a candidate drug delivery carrier and provided a new drug delivery strategy for actively targeted therapy of CKD.

Declaration of competing interest

The authors report no conflicts of interest in this work.

Acknowledgments

This research was financially supported by the National Natural Science Foundation of China (No. 81673363).

Appendix A. Supplementary data

Supplementary data to this article can be found online at https://doi.org/10.1016/j.biomaterials.2021.121053.

Data availability

The raw/processed data required to reproduce these findings cannot be shared at this time as the data also forms part of an ongoing study.

Credit author statement

Chengyuan Huang: Conceptualization, Methodology, Investigation, Writing - original draft, Software, Formal analysis, Data Curation. Xuan Zhao: Methodology, Writing - review & editing, Visualization. Meiling Su: Software, Formal analysis, Writing - review & editing. Zongning Yin: Writing - Review & Editing, Resources, Supervision, Project administration, Funding acquisition.

References

[1] K. Bruck, V.S. Stel, et al., Translational research in nephrology: chronic kidney disease prevention and public health, Clin Kidney J 8 (6) (2015) 647–655, https://doi.org/10.1093/ckj/sfv082.
[2] M. Gonzalez-Quiroz, N. Pearce, et al., What do epidemiological studies tell us about chronic kidney disease of undetermined cause in Meso-America? A systematic review and meta-analysis,, Clin Kidney J 11 (4) (2018) 496–506, https://doi.org/10.1093/ckj/sfx136.
[3] K.J. Foreman, N. Marquez, et al., Forecasting life expectancy, years of life lost, and all-cause and cause-specific mortality for 250 causes of death: reference and alternative scenarios for 2016–40 for 195 countries and territories, Lancet 392 (10159) (2018) 2052–2090, https://doi.org/10.1016/s0140-6736(18)31694-5.
[4] J.K. Ng, P.K. Li, Chronic kidney disease epidemic: how do we deal with it? Nephrology (2018) 116–120, https://doi.org/10.1111/nep.13464, 23 Suppl 4.
[5] J. Zhong, H.C. Yang, et al., A perspective on chronic kidney disease progression,, Am. J. Physiol. Ren. Physiol. 312 (3) (2017) F375–F384, https://doi.org/10.1152/ajprenal.00266.2016.
[6] P. Romagnani, G. Remuzzi, et al., Chronic kidney disease, Nat Rev Dis Primers 3 (2017) 17088, https://doi.org/10.1038/nrdp.2017.88.
[7] X. Zhao, D.Y. Hwang, et al., The role of glucocorticoid receptors in podocytes and nephrotic syndrome,, Nucl. Recept. Res. 5 (2018), https://doi.org/10.11131/2018/101323.
[8] J. Hogan, J. Radhakrishnan, The treatment of idiopathic focal segmental glomerulosclerosis in adults,, Adv. Chron. Kidney Dis. 21 (5) (2014) 434–441, https://doi.org/10.1053/j.ackd.2014.03.016.
[9] T.P. Andolino, J. Reid-Adam, Nephrotic syndrome, Pediatr. Rev. 36 (3) (2015) 117–126, https://doi.org/10.1542/pir.36-3-117.
[10] T.H. Tran, J H G, et al., Overview of current and alternative therapies for idiopathic membranous nephropathy, Pharmacotherapy 35 (4) (2015) 396–411, https://doi.org/10.1002/phar.1575.
[11] J.B. Rice, A.G. White, et al., Long-term systemic corticosteroid exposure: a systematic literature review,, Clin. Therapeut. 39 (11) (2017) 2216–2229, https://doi.org/10.1016/j.clinthera.2017.09.011.
[12] M. Oray, K. Abu Samra, et al., Long-term side effects of glucocorticoids, Expet Opin. Drug Saf. 15 (4) (2016) 457–465, https://doi.org/10.1517/14740338.2016.1140743.
[13] L. Buckley, M.B. Humphrey, Glucocorticoid-Induced osteoporosis, N. Engl. J. Med. 379 (26) (2018) 2547–2556, https://doi.org/10.1056/NEJMcp1800214.
[14] A. Caplan, N. Fett, et al., Prevention and management of glucocorticoid-induced side effects: a comprehensive review: gastrointestinal and endocrinologic side effects,, J. Am. Acad. Dermatol. 76 (1) (2017) 11–16, https://doi.org/10.1016/j.jaad.2016.02.1239.
[15] A. Caplan, N. Fett, et al., Prevention and management of glucocorticoid-induced side effects: a comprehensive review: ocular, cardiovascular, muscular, and psychiatric side effects and issues unique to pediatric patients,, J. Am. Acad. Dermatol. 76 (2) (2017) 201–207, https://doi.org/10.1016/j.jaad.2016.02.1241.
[16] F. Aljebab, I. Choonara, et al., Systematic review of the toxicity of long-course oral corticosteroids in children, PloS One 12 (1) (2017), e0170259, https://doi.org/10.1371/journal.pone.0170259.
[17] C.D. Borges, A.F. Dias, et al., Long-term adverse effects on reproductive function in male rats exposed prenatally to the glucocorticoid betamethasone, Toxicology 376 (2017) 15–22, https://doi.org/10.1016/j.tox.2016.04.005.
[18] N. Raval, A. Kumawat, et al., Understanding molecular upsets in diabetic nephropathy to identify novel targets and treatment opportunities, Drug Discov. Today 25 (5) (2020) 862–878, https://doi.org/10.1016/j.drudis.2020.01.008.
[19] J. Patrakka, K. Tryggvason, New insights into the role of podocytes in proteinuria, Nat. Rev. Nephrol. 5 (8) (2009) 463–468, https://doi.org/10.1038/nrneph.2009.108.
[20] C.P. Liu, Y. Hu, et al., Targeting strategies for drug delivery to the kidney: from renal glomeruli to tubules, Med. Res. Rev. 39 (2) (2019) 561–578, https://doi.org/10.1002/med.21532.
[21] M.A. Lal, K.W. Young, et al., Targeting the podocyte to treat glomerular kidney disease, Drug Discov. Today 20 (10) (2015) 1228–1234, https://doi.org/10.1016/j.drudis.2015.06.003.
[22] J.W. Leeuwis, T.Q. Nguyen, et al., Targeting podocyte-associated diseases, Adv. Drug Deliv. Rev. 62 (14) (2010) 1325–1336, https://doi.org/10.1016/j.addr.2010.08.012.
[23] H. Liu, X. Gao, et al., alpha-Actinin-4 is involved in the process by which dexamethasone protects actin cytoskeleton stabilization from adriamycin-induced podocyte injury, Nephrology 17 (8) (2012) 669–675, https://doi.org/10.1111/j.1440-1797.2012.01645.x.
[24] T. Wada, J.W. Pippin, et al., Dexamethasone prevents podocyte apoptosis induced by puromycin aminonucleoside: role of p53 and Bcl-2-related family proteins, J. Am. Soc. Nephrol. 16 (9) (2005) 2615–2625, https://doi.org/10.1681/ASN.2005020142.
[25] S. Agrawal, M.A. Chanley, et al., Pioglitazone enhances the beneficial effects of glucocorticoids in experimental nephrotic syndrome, Sci Rep 6 (2016) 24392, https://doi.org/10.1038/srep24392.
[26] R.F. Ransom, N.G. Lam, et al., Glucocorticoids protect and enhance recovery of cultured murine podocytes via actin filament stabilization, Kidney Int. 68 (6) (2005) 2473–2483, https://doi.org/10.1111/j.1523-1755.2005.00723.x.
[27] C. Kuppe, C. van Roeyen, et al., Investigations of glucocorticoid action in GN, J. Am. Soc. Nephrol. 28 (5) (2017) 1408–1420, https://doi.org/10.1681/ASN.2016010060.
[28] S. Yu, Y. Li, Dexamethasone inhibits podocyte apoptosis by stabilizing the PI3K/Akt signal pathway, Biomed Res Int 2013 (2013) 326986, https://doi.org/10.1155/2013/326986.
[29] F. Oroojalian, F. Charbgoo, et al., Recent advances in nanotechnology-based drug delivery systems for the kidney, J. Contr. Release 321 (2020) 442–462, https://doi.org/10.1016/j.jconrel.2020.02.027.
[30] R. Bruni, P. Possenti, et al., Ultrasmall polymeric nanocarriers for drug delivery to podocytes in kidney glomeruli, J. Contr. Release 255 (2017) 94–107, https://doi.org/10.1016/j.jconrel.2017.04.005.
[31] L. Wu, M. Chen, et al., Albumin-based nanoparticles as methylprednisolone carriers for targeted delivery towards the neonatal Fc receptor in glomerular podocytes, Int. J. Mol. Med. 39 (4) (2017) 851–860, https://doi.org/10.3892/ijmm.2017.2902.
[32] K. Tryggvason, J. Patrakka, et al., Mechanisms of disease: hereditary proteinuria syndromes and mechanisms of proteinuria, N. Engl, J. Med. 354 (13) (2006) 1387–1401, https://doi.org/10.1056/NEJMra052131.
[33] A. Remuzzi, S. Conti, et al., Role of ultrastructural determinants of glomerular permeability in ultrafiltration function loss, JCI Insight 5 (13) (2020), https://doi.org/10.1172/jci.insight.137249.
[34] W.L. Rice, A.N. Van Hoek, et al., High resolution helium ion scanning microscopy of the rat kidney, PLoS. One 8 (3) (2013), e57051, https://doi.org/10.1371/journal.pone.0057051.
[35] B. Deepa, C. Venkatraman Anuradha, Effects of linalool on inflammation, matrix accumulation and podocyte loss in kidney of streptozotocin-induced diabetic rats, Toxicol. Mech. Methods 23 (4) (2013) 223–234, https://doi.org/10.3109/15376516.2012.743638.
[36] Y.S. Kanwar, Continuum of historical controversies regarding the structural-functional relationship of the glomerular ultrafiltration unit, Am. J. Physiol. Ren. Physiol. 308 (5) (2015) F420–F424, https://doi.org/10.1152/ajprenal.00640.2014.
[37] E. Gagliardini, S. Conti, et al., Imaging of the porous ultrastructure of the glomerular epithelial filtration slit, J. Am. Soc. Nephrol. 21 (12) (2010) 2081–2089, https://doi.org/10.1681/ASN.2010020199.
[38] L. Perico, S. Conti, et al., Podocyte-actin dynamics in health and disease, Nat. Rev. Nephrol. 12 (11) (2016) 692–710, https://doi.org/10.1038/nrneph.2016.127.
[39] G.W. Liu, A.N. Prossnitz, et al., Glomerular disease augments kidney accumulation of synthetic anionic polymers, Biomaterials 178 (2018) 317–325, https://doi.org/10.1016/j.biomaterials.2018.06.001.
[40] G.W. Liu, J.W. Pippin, et al., Nanoparticles exhibit greater accumulation in kidney glomeruli during experimental glomerular kidney disease, Phys. Rep. 8 (15) (2020), e14545, https://doi.org/10.14814/phy2.14545.

[41] S. Schordan, E. Schordan, et al., AlphaV-integrins mediate the mechanoprotective action of osteopontin in podocytes, Am. J. Physiol. Ren. Physiol. 300 (1) (2011) F119–F132, https://doi.org/10.1152/ajprenal.00143.2010.
[42] J. Reiser, S. Sever, Podocyte biology and pathogenesis of kidney disease, Annu. Rev. Med. 64 (2013) 357–366, https://doi.org/10.1146/annurev-med-050311-163340.
[43] T. Madhusudhan, S. Ghosh, et al., Podocyte integrin-beta 3 and activated protein C coordinately restrict RhoA signaling and ameliorate diabetic nephropathy, J. Am. Soc. Nephrol. 31 (8) (2020) 1762–1780, https://doi.org/10.1681/ASN.2019111163.
[44] K. Pollinger, R. Hennig, et al., Kidney podocytes as specific targets for cyclo (RGDfC)-modified nanoparticles, Small 8 (21) (2012) 3368–3375, https://doi.org/10.1002/smll.201200733.
[45] Y. Ma, G. Ai, et al., Novel linear peptides with high affinity to alphavbeta3 integrin for Precise tumor identification, Theranostics.7(6) (2017) 1511–1523, https://doi.org/10.7150/thno.18401.
[46] S.A. Abouelmagd, N.H. Abd Ellah, et al., Self-assembled tannic acid complexes for pH-responsive delivery of antibiotics: role of drug-carrier interactions, Int. J. Pharm. 562 (2019) 76–85, https://doi.org/10.1016/j.ijpharm.2019.03.009.
[47] K. Shi, J. Li, et al., A pH-responsive cell-penetrating peptide-modified liposomes with active recognizing of integrin alphavbeta3 for the treatment of melanoma,, J. Contr. Release 217 (2015) 138–150, https://doi.org/10.1016/j.jconrel.2015.09.009.
[48] J. Wang, C. Poon, et al., Design and in vivo characterization of kidney-targeting multimodal micelles for renal drug delivery, Nano Research 11 (10) (2018) 5584–5595, https://doi.org/10.1007/s12274-018-2100-2.
[49] H. Zhang, J. Xu, et al., Self-assembled micelles based on Chondroitin sulfate/poly (d,l-lactideco-glycolide) block copolymers for doxorubicin delivery, J. Colloid Interface Sci. 492 (2017) 101–111, https://doi.org/10.1016/j.jcis.2016.12.046.
[50] X. Jin, P. Sun, et al., Star polymer-based unimolecular micelles and their application in bio-imaging and diagnosis, Biomaterials 178 (2018) 738–750, https://doi.org/10.1016/j.biomaterials.2018.01.051.
[51] P.M. Valencia, M.H. Hanewich-Hollatz, et al., Effects of ligands with different water solubilities on self-assembly and properties of targeted nanoparticles, Biomaterials 32 (26) (2011) 6226–6233, https://doi.org/10.1016/j.biomaterials.2011.04.078.
[52] M. Theerasilp, P. Chalermpanapun, et al., Imidazole-modified deferasirox encapsulated polymeric micelles as pH-responsive iron-chelating nanocarrier for cancer chemotherapy, RSC Adv. 7 (18) (2017) 11158–11169, https://doi.org/10.1039/c6ra26669j.
[53] D. Cai, W. Gao, et al., Hydrophobic penetrating peptide PFVYLI-modified stealth liposomes for doxorubicin delivery in breast cancer therapy, Biomaterials 35 (7) (2014) 2283–2294, https://doi.org/10.1016/j.biomaterials.2013.11.088.
[54] L. Zhang, W. Zheng, et al., Gene regulation with carbon-based siRNA conjugates for cancer therapy, Biomaterials 104 (2016) 269–278, https://doi.org/10.1016/j.biomaterials.2016.07.015.
[55] X. Yi, L. Chen, et al., Biomimetic copper sulfide for chemo-radiotherapy: enhanced uptake and reduced efflux of nanoparticles for tumor cells under ionizing radiation, Adv. Funct. Mater. 28 (9) (2018), https://doi.org/10.1002/adfm.201705161.
[56] C. Liu, W. Shan, et al., A novel ligand conjugated nanoparticles for oral insulin delivery,, Drug Deliv. 23 (6) (2016) 2015–2025, https://doi.org/10.3109/10717544.2015.1058433.
[57] E. Frohlich, The role of surface charge in cellular uptake and cytotoxicity of medical nanoparticles,, Int. J. Nanomed. 7 (2012) 5577–5591, https://doi.org/10.2147/IJN.S36111.
[58] A. Bera, A.K. Singh Chandel, et al., Degradable/cytocompatible and pH responsive amphiphilic conetwork gels based on agarose-graft copolymers and polycaprolactone, J. Mater. Chem. B 3 (43) (2015) 8548–8557, https://doi.org/10.1039/c5tb01251a.
[59] F. Chen, H. Hong, et al., Vivo tumor targeting and image-guided drug delivery with antibody-conjugated, radio conjugated mesoporous silica nanoparticles, ACS Nano 7 (10) (2013) 9027–9039, https://doi.org/10.1021/nn403617J.
[60] B. Du, M. Yu, et al., Transport and interactions of nanoparticles in the kidneys, Nat. Rev. Mater. 3 (2018) 358–374, https://doi.org/10.1038/s41578-018-0038-3.
[61] Y. Cheng, J.D. Meyers, et al., Deep penetration of a PDT drug into tumors by noncovalent drug-gold nanoparticle conjugates, J. Am. Chem. Soc. 133 (8) (2011) 2583–2591, https://doi.org/10.1021/ja108846h.
[62] N. Hoshyar, S. Gray, et al., The effect of nanoparticle size on in vivo pharmacokinetics and cellular interaction,, Nanomedicine 11 (6) (2016) 673–692, https://doi.org/10.2217/nnm.16.5.